

Texture Development and Plastic Deformation in a Pilgered Zircaloy-4 Tube

Jaiveer Singh¹, S. Mahesh², Gulshan Kumar¹, Prita Pant¹, D. Srivastava³, G. K. Dey³,
N. Saibaba⁴ and I. Samajdar¹

¹Department of Metallurgical Engineering & Materials Science, Indian Institute of Technology Bombay, Powai,
Mumbai-400 076, India

²Department of Aerospace Engineering, Indian Institute of Technology Madras, Chennai-600 036, India

³Materials Science Division, Bhabha Atomic Research Centre, Trombay, Mumbai-400 085, India

⁴Nuclear Fuel Complex, Hyderabad-500 062, India

Abstract:

The development of microstructure and crystallographic texture with effective strain at three through thickness locations (near rolls, center and near mandrel) in a partly pilgered Zircaloy-4 tube is described. Pilgering is found to eliminate through thickness variation in grain size in the starting hot extruded material, and to generate location dependent asymmetries in crystallographic texture. Deformation texture development during pilgering is modeled with polycrystal plasticity by idealizing the metal flow pattern as axisymmetric flow through a convergent channel. Good qualitative comparison of the predicted and experimental post-pilgering textures is obtained, provided location dependent transverse shear component is superposed on the gross flow field and localized deformation at grain boundaries is allowed. Frictional forces between tube and die are deduced from these observations.

Keywords: Zirconium, pilgering, plastic deformation, texture, anisotropy, microstructure, EBSD, polycrystal plasticity.

I. INTRODUCTION

The pilgering process, originated by the Mannesmann brothers [1–4], is an asymmetrical and non-monotonic incremental tube forming process, which can give high percentage reduction of both diameter and thickness of tubes with excellent control of dimensions [5,6]. The process involves repeated rolling of the tube over a mandrel using rolls (Fig. 1 (a)) with a tapered groove in their circumference [1–4]. Each pass is comprised of a forward stroke and a return stroke. The tube is pushed forward along its axis and turned about its axis before either the forward or return

stroke. Each rolling stroke involves 'biting', followed by reducing/forging and then polishing and idling [7–10]. The dimensions of the partly pilgered Zircaloy 4 tube is expected to trace the grooved rolls. Only a part of the inner surface of the tube, termed the groove, contacts the mandrel during the stroke. The remainder, which does not contact the mandrel, is called the flange. The turn about the tube axis given before each stroke ensures that different parts of the inner tube surface form the groove and flange in different passes. The imposed triaxiality of stresses or strains, which is intrinsic to pilgering, is known to offer better formability than typical draw bench operations [11–13].

Because it offers strong dimensional control, superior surface finish and controlled developments in deformed microstructure and crystallographic texture, pilgering is often used as the fabrication tool for a variety of critical components, e.g., zirconium alloy tubes used in thermal nuclear reactors [5,6,14,15]. Typically, hot extruded tubes are pilgered to achieve desired dimensions and microstructures/textures. The in-reactor performance of these components demands stringent quality control [16], which, in turn, demands detailed understanding of microstructure and property evolution during this complex incremental manufacturing process.

Efforts to quantify the microstructure and properties of zirconium alloy tubes produced by cold pilgering are described in the literature. Tenckhoff and Rittenhouse [17] characterized the final basal and prism pole figures and described the dependence of the texture and through thickness texture gradient on pilgering process parameters. Dressler et al. [18] obtained the yield locus of pilgered zirconium alloy tubes but did not correlate the properties with the manufacturing process variables. Kallstrom [19] conducted a critical examination of texture evolution as a function of pilgering strain. This work offers significant general insight but lacks an easily applicable macroscopic description of property evolution. Choi and Inoue [20] studied the effect of crystallographic texture and microstructure developed during pilgering on the corrosion resistance of the pilgered tube. Girard et al. [21] studied the influence of feeding rate, frequency of rolling steps and lubricant quality on the shear imposed in the pilgering-normal plane, which they then connected to the development of damage in the tube using a local approach. Guillen et al. [22] measured through thickness variation of the texture after five cold pilgering passes with an intermediate heat treatment step. They noticed and highlighted

asymmetry of the final pilgered texture along the tube transverse direction. Asymmetry has also been noticed in the experimental textures reported by other authors [22–25].

The crystallographic texture developed during pilgering significantly impacts in-service performance of pilgered zirconium alloy tubes also. It certainly impacts the yield anisotropy of the formed tube [18,25]. Also, irradiation creep, yield strength, hydride formation and stress corrosion cracking resistance strongly depend on the crystallographic texture [3]. Development of the basal (0001) fiber in zirconium alloy tubes during pilgering has an important influence on mechanical properties and on corrosion resistance, due to hydride formation in the basal plane [26–28]. Furthermore, in a multi-step fabrication process, the texture at the end of a pilgering step influences the formability of the next step. Finally, the internal stresses developed in the tube during pilgering are correlated with the texture [22,29]. These internal stresses can induce defects such as transverse cracks or surface damage, particularly at the inner tube surface [3].

Alongside experimental observations, many efforts reported in the literature have also been aimed at modeling the deformation and loading at a typical material. These can be classified as analytical or numerical (finite element method based). The approach of Furugen and Hayashi [30] belongs in the former category. They proposed a model of pilgering based on the theory of isotropic plasticity assuming Hencky's stress-strain relationship and the von Mises yield condition. In their model, the groove and flange are divided into two parts and axisymmetric deformation is enforced in each part. Their theory neglects shear stresses and strains. It predicts the evolution of normal stresses and strains through the process. Aubin et al. [31] developed a semi-analytical slab model of pilgering following the yield condition and flow rule of [30].

An important numerical study of the pilgering process is due to Montmitonnet, Aubin and co-workers. They modeled cold pilgering using the 3D finite element method [32–34]. These models account for the elastic and plastic deformation of the tube through an incremental elastic-viscoplastic constitutive law and also allow for consideration of the contact friction between rolls and tube. The complexity of the pilgering deformation itself and the complexity of the contact interactions between rolls, tube and mandrel render the full 3D finite element calculations computationally intractable. Efforts to keep the computations tractable lead to restrictive and

somewhat unrealistic assumptions [32]. Some of these restrictions persist despite the significant computational speed-up in simulations realized by Lodej et al. [34]. The difficulties associated with 3D numerical simulation have spurred approximate but more realistic modeling of the pilgering process using the 2D generalized plane strain finite element method [35].

In all the aforementioned efforts to model material deformation during pilgering, the material constitutive response is unrealistically assumed to be isotropic, even though a characteristic intense crystallographic texture develops [20,21,36]. This pilgering texture imparts significant anisotropy to the mechanical plastic response of the pilgered material [13,15]. The unrealistic material model assumed in the aforementioned works [30–35] makes the calculated deformation and load histories somewhat unreliable. Polycrystal plasticity [37,38] is an established methodology for predicting crystallographic texture evolution and anisotropic yield locus evolution during arbitrary plastic deformation. Lebensohn et al. [36] addressed texture evolution during pilgering with the viscoplastic self-consistent (VPSC) model. Modeling the imposed deformation during pilgering as monotonic compression along the radial and transverse directions and volume preserving extension along the axial direction, Lebensohn et al. [36] obtained acceptable predictions of the post-pilgering texture. Girard et al. [21] suggested the need for superposition of a shear component to improve the texture predictions. An important limitation of all polycrystal plasticity based pilgering simulations in the literature, which remains also in the present work, is that the non-monotonic unsteady deformation path imposed on a typical material point is not reliably known either from experiments or from process models, as described above. An approximate monotonic and steady deformation path based on changes in tube dimensions is therefore used in polycrystal plasticity modeling.

Though significant applied interests on pilgering of zirconium alloy tubes exist [6,20,21,23,39], comprehensive studies on microstructural developments during a single pilgering pass remain limited [24,40]. In the present work, experimental measurements of microstructure and texture at various locations along the pilgering stroke and through the thickness have been made for the first time (Sec. II). These measurements enable a cogent description of microstructure and texture *evolution* during a single pilgering pass. A location dependent asymmetry in texture development is observed, which is characterized by means of a scalar asymmetry parameter, A . Texture simulations using the binary tree based polycrystal

plasticity model are then reported (Sec. III). A novelty of these simulations is that in addition to accounting for the usual slip and twinning deformation modes within grains, the model allows for accommodative near grain boundary shears, consistent with experimental observations [41]. Comparing the simulated and experimental textures reveals that texture development is inconsistent with an axisymmetric flow field. Superposition of location dependent transverse simple shears is found necessary in order to explain the development of the texture asymmetry (Sec. IV). The variation of the frictional forces between the tube and the die along the pilgering stroke and the inner and outer diameters is suggested by these observations (Sec. V). It is found that the direction and magnitude of frictional shear stress is location dependent and that its amplitude must be comparable to the normal stresses.

II. EXPERIMENTAL METHOD

A single-phase Zircaloy-4 (for chemical composition, refer table 1) partly-pilgered tube is used in the present study. A schematic diagram of the pilgering process is shown in Fig. 1(a) [3]. A photograph of the partly-pilgered tube is given in Fig. 1 (b). Pertinent dimensions (in mm) are indicated in the accompanying sketch. PD, TD and ND denote the pilgering direction, the transverse direction, and the normal direction, respectively. The present study on a partly pilgered tube enables the direct observation of microstructural developments during progressing pilgering deformation: pilgering strain increases with axial distance from the start of the pilgering stroke at the left end, as indicated in Fig. 1 (b).

Samples for characterization through X-ray and electron diffraction are prepared by electropolishing [26]. This eliminates presence of near surface plastic deformation, which is typical of standard metallography. For electropolishing, a StruersTM Tenupol-5 system is used with 20:80 perchloric acid:methanol by volume at 20 V d.c. Macroscopic surface roughness caused by electropolishing is controlled by maintaining an electropolishing temperature of -20°C. Also, use of X-ray lens (PolycapTM) rules out defocusing from the electropolished surfaces. Electropolished surfaces were adequate for the EBSD patterns. Hence artifacts, from sample preparation affecting texture asymmetry can be ruled out.

Rectangular samples from the long transverse sections, containing the pilgering (PD) and normal (ND) directions, are used. It needs to be noted that the tube thickness varies, based on the

imposed strain, from 8 mm to 3 mm. A monochromatic Cu K α beam of 1mm \times 1mm is used for through thickness (near roll, centre and near mandrel) measurements. Such measurements are made for 10 different strains (or tube thickness) and three through-thickness locations (Fig. 1 (b)). Combinations of highly accurate Eulerian cradle (0.0001 $^\circ$ reproducibility) and multi-channel solid-state area detector (PixelTM) enable accurate pole figure measurements. Reproducibility is further ascertained by performing each measurement at least twice.

X-ray pole figure measurements are made on a PANalyticalTM X'Pert PRO MRD system. Standard Schulz method in reflection mode [42] is used for pole figure measurements. Four incomplete (maximum tilt angle: 85 $^\circ$) pole figures ($\{0002\}$, $\{10\bar{1}0\}$, $\{10\bar{1}2\}$, and $\{10\bar{1}3\}$) are measured. ODFs are then calculated by inversion of the pole figures using the Arbitrarily Defined Cells (ADC) Method [43]. Commercial software, LaboTex from LaboSoftTM, is used for the ODF calculations and plotting.

EBSD measurements are made in a FEITM Quanta 3D-FEG, using TSL-OIMTM EBSD software. In each sample, an area of 125 μm x 200 μm is covered at 0.1 μm step size. Beam and video conditions are otherwise kept identical between the scans. For the EBSD analysis, data with more than 0.1 CI (confidence index) is used. CI is a relative measure of statistical accuracy in automated EBSD indexing [44]. The X-ray diffraction and EBSD measurements are made at identical locations.

III. TEXTURE SIMULATIONS

A. Binary tree-based polycrystal plasticity model

Texture predictions are obtained from polycrystal plasticity simulations performed using the binary-tree based model [38]. In this model, grains are treated as homogeneously deforming rigid-plastic rate-independent domains. Further, aggregates of grains are represented as nodes of a binary tree, a standard data structure [45]. The lowest nodes of the binary tree represent grains. Higher binary tree nodes represent increasingly larger sub-aggregates of grains, culminating with the root of the tree (top most node), which represents the entire polycrystalline aggregate under consideration. Following standard terminology [45], the two nodes $[l(k)]$ and $[r(k)]$ that are 'descended' from a certain 'parent' node $[k]$ in the binary tree are called its 'children'. The two

child nodes $[l(k)]$ and $[r(k)]$ are then said to be ‘siblings’ of each other. The volume of the sub-aggregate represented by node $[k]$ is denoted $w_{[k]}$ in the sequel. It follows that

$$w_{[k]} = w_{[l(k)]} + w_{[r(k)]}. \quad (1)$$

The binary tree representation of the microstructure is exemplified schematically in a 4-grain microstructure in Fig. 2 (a). The corresponding binary tree is shown in Fig. 2 (b). In this example, node 3 is a parent of nodes C and D, which are siblings of each other. Sibling pairs in the present example are (A,2), (B,3) and (C,D). The root of this binary tree, which is shown at the top following standard convention [45], is node 1. This node represents the entire 4-grain aggregate.

In the binary-tree based model [38], field variables such as stresses $\sigma_{[k]}$ and strain-rates $\dot{\epsilon}_{[k]}$ of node $[k]$ are defined to be volume-fraction weighted averages of the corresponding fields over the children:

$$\sigma_{[k]} = \frac{\{w_{[l(k)]}\sigma_{[l(k)]} + w_{[r(k)]}\sigma_{[r(k)]}\}}{w_{[k]}}, \quad (2)$$

and

$$\dot{\epsilon}_{[k]} = \frac{\{w_{[l(k)]}\dot{\epsilon}_{[l(k)]} + w_{[r(k)]}\dot{\epsilon}_{[r(k)]}\}}{w_{[k]}}. \quad (3)$$

The lowest nodes of the binary tree are those with no child nodes. They are called leaves, and represent grains that obey the rigid-plastic rate-independent constitutive law [37]. Denoting the root of the tree by $[r]$, and the set of all leaf nodes that represent grains in the tree by G , it follows from Eqs. (2) and (3) that

$$\sigma_{[r]} = \sum_{[g] \in G} \sigma_{[g]}, \quad (4)$$

and

$$\dot{\epsilon}_{[r]} = \sum_{[g] \in G} \dot{\epsilon}_{[g]}. \quad (5)$$

The height of node $[k]$ will be important in the sequel. It is defined as [38]

$$h([k]) = 1 + \max(h(l[k]), h(r[k])), \text{ if } k \notin G, \text{ and} \quad (6)$$

$$h([k]) = 1, \text{ if } k \in G.$$

Fig. 3 shows a balanced binary tree [38] representing $2^3 = 8$ grains. The total number of nodes in this balanced binary tree is $2^4 - 1 = 15$, and the height of the root node is $1 + \log_2 8 = 4$.

In the binary-tree based model, the interface between the sub-aggregates represented by sibling nodes in the binary tree is assumed to be planar. Let the planar interface between the sibling nodes $[l(k)]$ and $[r(k)]$ be oriented normal to $\nu_{[k]}$.

Continuity of traction and velocity are imposed between sibling nodes across this planar interface. Thus,

$$\{\sigma_{[l(k)]} - \sigma_{[r(k)]}\} \cdot \nu_{[k]} = 0, \quad (7)$$

and

$$\dot{t}_{[k]} \cdot \{\dot{\varepsilon}_{[l(k)]} - \dot{\varepsilon}_{[r(k)]}\} \cdot t_{[k]} = 0, \forall t_{[k]} \perp \nu_{[k]}. \quad (8)$$

Eqs. (7) and (8) represent the most significant departure of the binary-tree based model from mean-field based polycrystal plasticity models, such as the Taylor [46], or the viscoplastic self-consistent model [47]; the binary-tree based model directly accounts for interaction between grains. However, all intergranular interactions are not directly accounted for in the binary-tree based model, unlike e.g., in the crystal plasticity finite element method. In the example of Fig. 2 (a), even though grain pairs (A, B), (B, C) or (B, D) have a common grain boundary, they interact somewhat indirectly in the binary-tree based model. For instance, the continuity conditions between grain pair (A, B) is subsumed within the interaction of grain A with sub-aggregate 2, of which grain B is a constituent. This reduction in the number of modeled interactions underlies the computational comparability of the binary-tree based model to the classical Taylor model [38].

Lattice rotations of grains and larger sub-aggregates in the binary tree based model are determined by compatibility with their sibling nodes. Detailed treatment of lattice rotations is given in [38].

B. Grain plasticity

The h.c.p. grains of present interest are assumed to have the following deformation modes: prismatic slip $(1010) \langle 1120 \rangle$, pyramidal slip $\{1011\} \langle 1123 \rangle$, extension twinning $\{1012\} \langle 1011 \rangle$ and contraction twinning $\{1122\} \langle 1123 \rangle$ following e.g., Tenchoff [5] and Tomé et al. [48]. The latter two twinning modes entail a transformation of the lattice orientation of the grain.

Activation of twinning systems and accommodation of shear by their activation entails a transformation of the lattice orientation of the grain matrix [37,49]. The volume fraction f_t of twin variant t depends on the accumulated shear γ_t in twinning system t and its characteristic twinning shear, Γ_t as:

$$f_t = \gamma_t / \Gamma_t. \quad (9)$$

In zirconium [37,49], it is known that $\Gamma_t = 0.169$ for the six variants of $\{1122\} \langle 1123 \rangle$ extension twins and that $\Gamma_t = 0.225$ for the six variants of $\{1122\} \langle 1123 \rangle$ contraction twins. If the volume fraction of twin variant t exceeds a pre-set threshold, i.e., if $f_t \geq f_0 = 0.8$, the lattice orientation of the parent grain is completely reoriented to that of twin variant t . In parallel with γ_t , the accumulated shear in slip system s is denoted γ_s .

Following Chin et al. [50], it is assumed that twinning occurs when the resolved shear stress in a twinning system exceeds its critical resolved shear stress. More recent observations [51,52], suggest that twinning is nucleated in hard grains by prismatic dislocations in neighboring soft grains activating twin nuclei at grain boundaries. This mechanism is not modeled presently.

C. Near grain boundary accommodation

In the binary-tree based polycrystal plasticity model [38], as noted in Sec. III A, grains are assumed to deform homogeneously and continuity of tractions and velocity components is enforced between the sub-aggregates representing sibling nodes of the binary tree. This assumption implies that near-grain boundary localized deformation is negligible. The homogeneity of grain deformation, as assumed in the binary-tree based model is a reasonable representation of the physical continuity between neighboring grains, when the plastic strain is significantly greater than the elastic strain in high symmetry materials such as f.c.c. pure copper [53]. On the other hand, in low symmetry h.c.p. materials, intense grain boundary strains orders of magnitude larger than grain bulk strains develop [54–56]. The large grain boundary shears are a consequence of the intense stress concentrations developed near grain boundaries required to maintain compatibility between grains that have fewer than five independent easily activated slip systems [57]. These stress concentrations activate deformation modes near grain boundaries, which are not activated in the grain bulk [57]. Examples of near grain boundary slip modes reported in the literature in zirconium alloys at room temperature are $\{11\bar{2}3\}$ slip [58], basal slip [59], and more profuse activation of pyramidal $\langle c + a \rangle$ slip. Refs. [57,60] report enhanced $\{11\bar{2}3\}$ twinning activity near grain boundaries.

In order to allow grain boundary accommodation of incompatible deformation within the binary-tree based model, stresses $\sigma_{[k]}$ and strain-rates $\dot{\epsilon}_{[k]}$ are regarded as fields in the bulk of the sub-aggregate $[k]$. The sub-aggregate boundary is comprised of grain boundaries that fall on the surface of the sub-aggregate. The stress and strain-rate fields within the sub-aggregate boundaries are expected to be highly inhomogeneous and generally of larger magnitude than $\sigma_{[k]}$ and $\dot{\epsilon}_{[k]}$.

In the present work, grain boundary accommodation between sub-aggregates represented by the children of node $[k]$ is accounted for by relaxing the velocity continuity condition, Eq. (8) at node $[k]$. Then, the strain-rates of the sub-aggregates represented by the sibling nodes $[l(k)]$ and $[r(k)]$ will, in general, be incompatible. It is assumed that grain boundary shears accommodate the incompatibility in the strain-rates, by activating one or more grain boundary deformation modes noted in the preceding paragraph. It should be noted that under this assumption, the grain boundary shears merely serve to restore compatibility between

incompatibly deforming sub-aggregates; the macroscopically imposed deformation is still accommodated only by the deformation of the grain bulks following Eqs. (4), and (5). It is shown in [38] that if Eq. (8) is relaxed at node $[k]$ of the binary tree,

$$\sigma_{[l(k)]} = \sigma_{[r(k)]}. \quad (10)$$

If the volume of the near grain boundary region is neglected in comparison with that of grain bulk, the grain boundary accommodation process will add negligible plastic power to that of the bulk. This assumption, although somewhat unrealistic, is presently made. A better approach to dealing with grain boundary accommodation has been offered by Engler et al. [61]. In that approach, the dislocation density required for restoring material compatibility is determined and the associated stored energy is accounted for.

The present work is concerned with a balanced binary tree model of the polycrystal (e.g., Fig. 3). Near grain boundary shear between pairs of grains in this model is allowed by enforcing Eq. (10) at all nodes $[k]$ that satisfy $h([k]) = 2$. Grain boundary shears between pairs of sub-aggregates each, in turn, comprised of a pair of grains is ensured by enforcing Eq. (10) at all nodes $[k]$ that satisfy $h([k]) \leq 3$, and so on. Thus, in general, substituting Eq. (10) in lieu of the compatibility conditions given by Eqs. (7), and (8) at nodes $[k]$ that satisfy

$$h([k]) \leq H, \quad (11)$$

amounts to allowing near grain boundary shears between sub-aggregates up to height H .

Eqs. (10), and (11) together imply that a balanced binary tree based model polycrystal is essentially a collection of compatibly deforming sub-aggregates. Each sub-aggregate is comprised of 2^{H-1} grains. The stress within each sub-aggregate of 2^{H-1} grains is uniform; i.e., each sub-aggregate satisfies the Sachs assumption [62]. Since Sachs polycrystals tend to deform highly inhomogeneously [37], the present methodology for treating near grain boundary shear will enhance strain localization within soft grains.

Experimental observations of near grain boundary deformation go back at least to Hauser et al. [41]. Its modeling is, however, more recent. Staroselsky and Anand [63] were, to our

knowledge, the first to account for near grain boundary deformation in a model. In order to predict reasonable values stresses in a magnesium alloy, they found it necessary to model grain boundary shear using an isotropic plasticity model in a ‘grain boundary layer’.

D. Material point deformation

Unlike in simple processes such as channel die compression, or uniaxial tension, the geometry of the pilgering process does not readily suggest the deformation imposed upon the tube. In fact, the deformation imposed on a typical material point in the tube is non-axisymmetric, unsteady, and dependent on the location of the material point.

Let $v_i(x_k)$ denote the material flow velocity at spatial coordinate x_k . Let

$$L_{ij}(x_k) = \frac{\partial v_i}{\partial x_k}; i, j \in \{PD, TD, ND\} \quad (12)$$

denote the velocity gradient at spatial coordinate x_k . The geometry of the pilgering process does suggest certain zero components of the velocity gradient. Treating the mandrel as rigid, continued contact between the groove and the mandrel requires (Fig. 1):

$$\frac{\partial v_{ND}}{\partial x_{PD}} = L_{ND,PD} = 0, \quad (13)$$

and

$$\frac{\partial v_{ND}}{\partial x_{TD}} = L_{ND,TD} = 0. \quad (14)$$

Pilgering simultaneously reduces the diameter and thickness of the tube. As noted above, the reductions are not monotonic. Regarding the reductions of diameter and thickness as monotonic and linear functions of imposed strain, therefore, represents a significant idealization of the actual process. This assumption amounts to approximating pilgering as extrusion through a converging channel. Assuming a linear reduction of both diameter and thickness, and requiring volume conservation during plastic deformation of the tube yields:

$$\frac{\partial v_{TD}}{\partial x_{TD}} = L_{TD,TD} = -1, \quad (15)$$

$$\frac{\partial v_{ND}}{\partial x_{ND}} = L_{ND,ND} = -Q, \quad (16)$$

and,

$$\frac{\partial v_{PD}}{\partial x_{PD}} = L_{PD,PD} = 1 + Q. \quad (17)$$

The value of Q depends on the location of the material point before and after the pilgering process. Let R_0 and r_0 denote the outer and inner tube radii measured from the mandrel centerline before pilgering and let R and r denote the same after pilgering. The engineering definition of Q is then (Allen et al. [15]):

$$Q_{\text{eng}} = \frac{1}{2} \left(1 - \frac{R - r}{R_0 - r_0} \right). \quad (17)$$

Through-thickness location dependent Q_{eng} are obtained by regarding the tube as being divided into a number of co-axial cylinders and by applying Eq. (17) to each cylinder, as detailed by Allen et al. [15].

Q_{eng} is a realistic measure of the true deformation only over infinitesimal pilgering reductions. Over finite reductions, Abe et al. [64] give

$$Q = \log \left[\frac{R_0^2 - r_0^2}{R^2 - r^2} \right] / \log \left[\frac{\rho_0}{\rho} \right] - 1. \quad (18)$$

Here, ρ_0 and ρ denote the radial distance of the material point under consideration from the mandrel centerline before and after the deformation, respectively. The true Q given by Eq. (18) is therefore, intrinsically through-thickness location dependent. A large $Q \gg 1$ implies that the

deformation is nearly plane strain in PD-ND plane. On the other hand, a small $Q \ll 1$ indicates plane-strain like deformation in the PD-TD plane. $Q \approx 1$ indicates deformation conditions similar to uniaxial extension along PD.

Velocity gradient components $L_{TD,ND}$, $L_{PD,ND}$, $L_{TD,PD}$ and $L_{PD,TD}$ are not directly suggested by the process geometry. They are, therefore, presently regarded as unknowns and the velocity gradient matrix in the PD-TD-ND system is taken to be:

$$[L]_{PD-TD-ND} = \begin{bmatrix} 1 + Q & L_{PD,TD} & L_{PD,ND} \\ L_{TD,PD} & -1 & L_{TD,ND} \\ 0 & 0 & -Q \end{bmatrix}. \quad (19)$$

The diagonal components of the velocity gradient produce the changes in the tube dimensions observed after pilgering. They may therefore be termed the effective components of the velocity gradient. The geometry of the pilgering process, however, does not preclude non-zero values for four of the off-diagonal components, which may therefore be termed the redundant components.

In terms of the velocity gradient given in Eq. (19), the von Mises effective strain-rate is defined exclusively in terms of the effective components as [3]:

$$\dot{\bar{\epsilon}} = \sqrt{\frac{2}{3} \{L_{PD,PD}^2 + L_{TD,TD}^2 + L_{ND,ND}^2\}}. \quad (20)$$

The effective strain experienced by a material point is then defined as the time integral of the effective strain-rate over its loading history:

$$\bar{\epsilon}(t) = \int_0^t \dot{\bar{\epsilon}}(t') dt'. \quad (21)$$

The velocity gradient assumed in the simulations of Lebensohn et al. [36] is that given by Eq. (19) with all off-diagonal terms are assumed zero. Their flow field therefore amounts to neglecting all but the effective components. Girard et al. [21] measured the off-diagonal components using an insert technique and found that $L_{PD,ND}$ is much larger than other off-diagonal components. They found that their predictions were improved by consideration of the $L_{PD,ND}$ component.

IV. SCALAR TEXTURE DESCRIPTORS

Texture descriptions are made convenient by the introduction of the following two scalar descriptors:

A. Kearns factors

The nuclear industry often uses Kearns factors [65], also called f factors, to quantify texture development in zirconium alloys [28,66–69]. f -factors represent the fraction of basal poles oriented near a reference direction:

$$f = \int_0^{\frac{\pi}{2}} I_{\theta} \sin \theta \cos^2 \theta \, d\theta, \quad (22)$$

where $I_{\theta} \sin \theta$ is the volume fraction of the grains with their c-axes oriented at a tilt angle θ from the reference direction, expressed in units of times random [70]. The reference directions in the present study are taken to be the pilgering direction (PD), transverse direction (TD) and radial or normal direction (ND) of the tube. The Kearns factors are thus summary descriptors of the texture in terms of three scalar quantities. Nagai et al. [71] obtained correlations between the f -factors and the pilgering process parameter Q using a regression scheme over seven process paths. They also quantified the texture gradient along the wall thickness, and attributed it to variation of Q with through-thickness material point position. Konishi et al. [72] quantified the texture evolution along the pilgering stroke in terms of the f -factors and proposed a simple model based on the local radial and circumferential strain ratio to explain it. They also noted the influence of the area reduction factor on f -factors in as-rolled tubes, and obtained general correlations between the f -factors, Q , and the tube area reduction.

B. Asymmetry parameter

Barring a few exceptions e.g., [21,36], much of the experimental pilgering texture reported in the literature is presented after symmetrizing according to orthonormal sample symmetry [73] Pilgering being a non-axisymmetric, non-monotonic, unsteady deformation process [30], the assumption of orthonormal symmetry is not justified. In the present work, therefore, orthonormal sample symmetry is not invoked. On the contrary, it will be shown that

the asymmetries in the texture evolution evolve systematically with pilgering deformation. In order to compactly represent the evolution of asymmetry, an asymmetry parameter, A , is defined:

$$A = \int_R f(\varphi_1, \varphi, \varphi_2) dg - \int_L f(\varphi_1, \varphi, \varphi_2) dg. \quad (23)$$

The volume element dg in orientation space is given by [73]:

$$dg = \left(\frac{\sin \varphi}{8\pi^2} \right) d\varphi_1 d\varphi d\varphi_2. \quad (24)$$

In Eq. (9), the regions of integration R and L divide the orientation space into two equal parts:

$$R = \{(\varphi_1, \varphi, \varphi_2): 90^\circ \leq \varphi_1 \leq 270^\circ; 0^\circ \leq \varphi \leq 90^\circ; 0^\circ \leq \varphi_2 \leq 60^\circ\}, \text{ and} \quad (25)$$

$$L = \{(\varphi_1, \varphi, \varphi_2): 0^\circ \leq \varphi_1 < 90^\circ; 0^\circ \leq \varphi \leq 90^\circ; 0^\circ \leq \varphi_2 \leq 60^\circ\}$$

$$\cup \{(\varphi_1, \varphi, \varphi_2): 270^\circ < \varphi_1 \leq 360^\circ; 0^\circ \leq \varphi \leq 90^\circ; 0^\circ \leq \varphi_2 \leq 60^\circ\}.$$

Region L is shown hatched in a $\varphi_2 = \text{constant}$ section and in the (0002) pole figure in Fig. 4; the remainder represents R . The two terms on the right hand side of Eq. (9) are thus the total texture weight near the $\langle 1\bar{1}00 \rangle$ fiber and the $\langle \bar{1}100 \rangle$ fibers, respectively. The asymmetry parameter A thus quantifies the imbalance in the texture weight of these two fibers. Orthotropic symmetry implies $A = 0$.

Texture asymmetry, or deviation from orthorhombic symmetry, has also been reported in the literature in processes ranging from pilgering [22] to asymmetric rolling [74]. Shear dictates the developments of such asymmetries. Shear, for example, is shown [21] as essential to predict textural developments during pilgering. Differences in the imposed friction can affect through thickness texture developments even during rolling [75].

The asymmetry parameter A , and the ND Kearns factor f are complementary descriptors of the texture. In the computation of the ND Kearns factors, $+ND$ and $-ND$ are equivalent directions. This follows from Eq. (22) and the identity $\sin(180^\circ - \theta) = \sin \theta$. On the other hand, A

discriminates between $+ND$ and $-ND$ (Eq. (23) and Fig. 4). As an extreme example, consider two polycrystals. Let the basal poles of all grains of the first polycrystal be aligned about $-ND$. Let the basal poles of 50% (by volume) of grains of the second polycrystal be aligned along $-ND$, and let the basal poles of the remaining grains be aligned along $+ND$. The ND Kearns factor of both polycrystals is 1. However, the asymmetry parameter A of the first polycrystal is -1 , while that of the second is zero.

V. RESULTS

A. Experimental

1. Microstructural Developments

Measurements are made at the various distances from the start of the pilgering stroke, shown in Fig. 1 (b). At each measurement section, average outer and inner diameters are measured. These dimensions, when substituted into Eqs. (17), (18), and (21), yield the variation of the effective strain $\bar{\epsilon}$, Q_{eng} , and Q , plotted in Fig. 5 (a), (b), and (c), respectively. The calculations assume that the velocity gradient $[L]_{[PD-TD-ND]}$ remains uniform between two measurement sections. It is clear from Fig. 5 (c), that Q may have large variations along both PD and ND.

EBSD analysis shows that the starting hot extruded and annealed ‘mother-hollow’ tube has significant differences in grain size between different through thickness locations (Fig. 6, first row). Identifying a grain as a region in the EBSD micrograph surrounded by a continuous boundary of misorientation in excess of 5° , it is found that the near roll section of the extruded tube has finer grains ($\sim 8 \mu\text{m}$) before pilgering than elsewhere ($\sim 18 \mu\text{m}$ for the center and near mandrel sections); see Fig. 7 (a). Progressive deformation brings concurrent microstructural developments, also shown in Figs. 6 and 7. The pilgered grains are elongated along PD and reduced along ND. Further elongation of grains ceases beyond about 200 mm from the start of the pilgering stroke (Fig. 7 (b)). Existence of fine grains and non-indexed regions ($CI < 0.1$) is also apparent (Fig. 7 (c)). Intense microstructural refinement may be associated with confidence index $CI < 0.1$. It is seen from Fig. 7 (c) that microstructural refinement is highest at the center, and least at the near mandrel section. Finally, in-grain misorientation development is quantified using the grain average misorientation or GAM value. GAM represents average point-to-point

misorientation inside an EBSD grain. As shown in Fig. 7 (d), the original hot extruded microstructure had nearly identical through thickness GAM values. Progressive pilgering increased the GAM at all three locations. However, GAM at near roll and near mandrel sections are somewhat higher than that at the center.

2. Crystallographic texture development

Experimentally measured basal (0002) pole figures measured at various effective strains are shown in Fig. 8. The corresponding orientation distribution functions (ODF) calculated from the measured (0002), (10 $\bar{1}$ 0), (10 $\bar{1}$ 2), and (10 $\bar{1}$ 3) pole figures are shown in Fig. 9. Following previous work [40], the ODF section at $\varphi_2 = 30^\circ$ is used representatively.

As shown in both Figs. 8 and 9, the starting material had a non-random texture with well-defined fibers. Deformation resulted in gradual texture developments. With increasing effective strain $\bar{\epsilon}$, texture intensities along the $\langle 1\bar{1}00 \rangle$, and $\langle \bar{1}100 \rangle$ fibers increase. A large increase in texture intensities occurs at all three sections between 200 mm to 320 mm, with a relatively small increase in effective strain $\bar{\epsilon}$, toward the end of pilgering.

The Kearns factors (f -factors), defined in Eq. (21), are often used to quantify texture development in zirconium alloy tubes. As shown schematically in Fig. 10 (a), f -factor values represent the fraction of basal poles in one of the three principle directions. Figs. 10 (b-d) show the radial (reference direction = ND), axial (reference direction: PD) and circumferential (reference direction: TD) f -factors, respectively. At all three through-thickness sections, radial Kearns factors show an increasing trend, while the axial and circumferential Kearns factors decrease during pilgering. This indicates that on average, grains rotate during pilgering and align their c -axes closer to ND and away from PD and RD; this is also seen from Figs. 8 and 9.

A large change in all three f -factors is observed between 0 mm to 35 mm of the pilgering stroke in Figs. 10 (b-d). While the radial f -factor increases abruptly in this early part of the pilgering stroke, the axial and circumferential f -factors show a steep decrease. It is believed that these abrupt variations are due to ‘biting’, which occurs at the start of the pilgering stroke in standard manufacturing practice. During ‘biting’, the inhomogeneous deformation may be imparted to the tube draft in order to position it within the gap between the rolls and the mandrel, at least part of which is through-thickness.

The abrupt change in the f factors between 0 mm to 35 mm of the pilgering stroke is not due to intense contraction twinning during the ‘biting’ phase. As will be shown later (Sec V B. 2a), contraction twinning will generate twins whose c -axes are aligned close to PD. This will result in an increase of the axial Kearns factor. The contrary is, however, observed in experimental measurements shown in Fig. 10 (c).

Fig. 11 plots the asymmetry parameter, A , defined in Eq. (23), as a function of pilgering position at all three through-thickness sections. Barring the first step of the present pilgering measurements between 0 mm to 35 mm, wherein tube ‘biting’ likely induces severe heterogeneities in the flow field (Sec. 2. A.), $|A|$ increases monotonically with effective strain $\bar{\epsilon}$ at all the through-thickness sections (Fig. 11). Comparable A , albeit of opposite signs, develop at the near rolls and near mandrel sections and a small A develops at the center section.

The development of texture asymmetry may also be observed directly from the pole figures (Fig. 8) or orientation distribution functions (ODFs) (Fig. 9). The near rolls section shows more ODF intensities in the $+ND$ while the near mandrel section offered $-ND$ ODF asymmetry. As explained at the end of Sec. IV, the Kearns factor description of texture cannot capture texture asymmetry; Fig. 10 shows that Kearns factor evolves similarly at all three through-thickness sections.

Texture asymmetry is often related to the fabrication process [70]. Rolling without redundant shear, for example, produces the orthorhombic or orthotropic symmetry. Redundant shear, on the other hand, produces asymmetry [76]. Information about the development of asymmetries, may offer significant clues about the nature of frictional forces acting on the tube, as discussed further in Sec. VI.

B. Simulations

1. Crystallographic texture

Following the methodology given in Sec. IV, texture predictions are made for three mesoscale material points at the near roll, center and mandrel sections. The initial textures are obtained by discretizing the X-ray bulk textures measured in the hot extruded tube into $2^{12} = 4096$ lattice orientations (model ‘grains’), each of volume fraction 2^{-12} . These lattice

orientations are assigned to the lowest nodes of a balanced binary tree model (e.g., Fig. 3) of the polycrystal [38], comprised of $2^{13} - 1 = 8191$ nodes. The experimentally observed initial texture and the discretized initial texture assumed in the simulations are compared in Fig. 12. Discretization is seen to marginally affect the scalar descriptors, even though the overall texture is qualitatively well captured. The normal to the $2^{12} = 4096$ planar interfaces between sub-aggregates in the model are initialized to vectors drawn randomly from a uniform distribution over the unit sphere. The texture predictions reported below are not affected by the specific choice of the set of random orientations.

As stated in Sec. III B, prismatic slip, pyramidal slip, extension twinning and contraction twinning are the allowed microscopic deformation modes in these model grains. The absolute values of the critical resolved shear stresses associated with these modes are presently irrelevant; only their ratio matters. The ratio of prismatic slip, pyramidal slip, extension twinning and contraction twinning modes is taken as 9:90:11:11. Thus, pyramidal slip is taken to be much harder than other slip or twinning deformation modes, in accord with experimental observations [48,60].

At each of the three through-thickness sections, all the components of the velocity gradient given by Eq. (15) are imposed on the root node $[r]$ of the binary tree

$$L_{[r]} = L_{\{PD-TD-ND\}}. \quad (26)$$

The deformation history imposed on the model polycrystal, given by Eqs. (25), and (18), tracks the experimental Q evolution shown in Fig. 5 (c). Texture predictions are obtained by imposing only the effective components of the velocity gradient in Eq. (18), i.e., by setting

$$L_{TD,ND} = L_{PD,ND} = L_{TD,PD} = L_{PD,TD} = 0. \quad (27)$$

Strict compatibility following Eq. (8) across all binary tree interfaces is enforced in the present simulation.

The predicted $\varphi_2 = 30^\circ$ ODF section at the center section is shown in Fig. 13 (a1), and the corresponding (0002) and (10 $\bar{1}$ 0) pole figures are shown in Fig. 13 (a2). Although the (0001), $\langle 1\bar{1}00 \rangle$, and $\langle \bar{1}100 \rangle$ fibers are captured by the simulations, the predictions compare poorly with experimental observations shown in Fig. 9 (b1). The most noticeable disagreement is that a significant textural intensity is predicted at $\varphi_1 = \frac{\pi}{4}$, $\varphi = \frac{\pi}{2}$, and at

$\varphi_1 = \frac{3\pi}{4}, \varphi = \frac{\pi}{2}$. These correspond to grains whose c -axes are nearly aligned with PD (Fig. 13 (b1)) and come from orientations formed by contraction twinning. This contradiction implies that contraction twinning is not a wide spread deformation mode in the present material. This conclusion agrees with previous works on a similar material [77,78], wherein microscopic investigations did not reveal contraction twins.

The accumulated shear per grain in a particular slip or twinning system s , is defined as

$$S_s = \frac{\sum_{k \in G} \gamma_s w_{[k]}}{\sum_{k \in G} w_{[k]}}. \quad (28)$$

Fig. 13 (a3) shows the evolution of $\sum_s S_s$; the summation over s runs over all the slip or twinning systems of the four deformation modes: prismatic slip, extension twinning, pyramidal slip and contraction twinning. It can be seen that on average, pilgering deformation is accommodated by prismatic slip and contraction twinning, and by extension twinning to a smaller degree. Negligible slip in the hard $\langle c + a \rangle$ pyramidal slip systems is predicted. The total slip and twin shear accumulated in the grains of the model polycrystal at the end of pilgering follows a nearly Gaussian distribution with mean value 4.6 and standard deviation 0.5, as shown in Fig. 13 (a4). The small standard deviation indicated that deformation is distributed evenly over all grains.

2. Microscopic mechanisms

The influence of three mechanisms on the predicted final pilgered texture is now investigated. These are: (a) The role of contraction twinning; (b) The role of near grain boundary shear; and (c) The role of redundant shears. Their individual and combined influences are investigated by turning each of these on or off in the simulations.

a. Absence of contraction twinning

The effect of suppressing the activation of contraction twinning is now studied. Here and in the sequel, the results of polycrystal plasticity simulations performed allowing only the

prismatic and pyramidal slip modes and extension twinning mode are reported. The present set of assumed deformation modes are in accord with the dislocation observed through electron microscopy by Numakura et al. [79]. As in Sec. V B 1., only the effective components of the velocity gradient are imposed. Fig. 13 (b1) shows the final predicted $\varphi_2 = 30^\circ$ ODF section. In contrast with Fig. 13 (a1), no textural intensity is predicted at $\varphi_1 = \frac{\pi}{4}$, $\varphi = \frac{\pi}{2}$, and at $\varphi_1 = \frac{3\pi}{4}$, $\varphi = \frac{\pi}{2}$, because contraction twinning, which generates these orientations has been turned off. The predicted post-pilgering texture can nevertheless not be said to agree, even qualitatively, with the experimental texture: The predictions are missing the basal (0001) fiber prominent in the experimentally observed Fig. 9 (b1). The rotation of grains away from the basal orientation is due to the activation of considerable $\langle c + a \rangle$ pyramidal slip.

As shown in Fig. 13 (b3), significant slip is associated with all the allowed deformation modes: prismatic slip, extension twinning and pyramidal slip. In the absence of contraction twinning, significant $\langle c + a \rangle$ pyramidal slip is required to accommodate contraction along the c –axis of grains. This occurs in order to enforce compatibility between sibling sub-aggregates in the binary tree model, despite the severe plastic power penalty associated with activating the extremely hard pyramidal slip systems.

The distribution of accumulated slip and twinning shears in the grains with contraction twinning is suppressed is not Gaussian, as it lacks symmetry about the mean value of 5.2. As shown in Fig. 13 (b4); the distribution is skewed toward higher accumulated shears. This is because certain grains, which are favorably oriented, deform much more than the sample mean. Others, which are unfavorably oriented, deform much less. The suppression of contraction twinning thus markedly accentuates the plastic anisotropy of the h.c.p. grains, which underlies the difference in the distribution of accumulated shear between Figs. 13 (a4) and (b4).

b. Near grain boundary deformation

Texture predictions obtained from simulations with only the effective components of the velocity gradient imposed, Eq. (19), but allowing for near grain boundary shear following Eqs. (10), and (11) with $H = 2$, and 3 are shown in Fig. 14 (a1), and (b1), respectively. Only the

predictions for the center section are shown. The case $H = 1$ is shown in the second column of Fig. 13.

The allowance of near grain boundary shear with $H = 2$ dramatically increases the (0001) fiber texture intensity. This is because the allowance of near grain boundary shear reduces the compatibility requirements between grains, which in turn, suppress all but easy prismatic slip in the grains (Fig. 14 (a2)). Grain deformation becomes more inhomogeneous than in the case of $H = 1$, with contraction twinning allowed, as seen by comparing Figs. 14 (a3) and 13 (a4): The mean and standard deviation of the accumulated shear distribution corresponding to $H = 2$ are 6.3, and 2.8, respectively. The inhomogeneous deformation also results in a quantitative change: greater intensities are now predicted along the $\langle 1\bar{1}00 \rangle$, and $\langle \bar{1}100 \rangle$ fibers than with $H = 1$. Further increase to $H = 3$ results in still greater intensification of three texture fibers (Figs. 14 (b1-b2)). However, as seen from Fig. 14 (b3), about 13% of grains are now predicted to hardly deform. In the micrographs shown in Fig. 6, however, all grains are seen to elongate. For this reason, the predictions obtained with $H = 3$ are not deemed physically representative of the actual near grain boundary deformation conditions. The same conclusion could also be expected to hold for all $H \geq 3$.

The observation of non-deforming grains in the $H = 3$ simulations has been dismissed presently as being physically unrealistic. This need not always be the case: E.g., Sahoo et al. [80] observed non-deforming grains in single phase Zircaloy-2 samples rolled to 50% strain monotonically. The absence of non-deforming grains in the present microstructure is likely due to the non-monotonicity of the deformation path during pilgering.

c. Redundant shears

Texture predictions at the near roll, center, and near mandrel sections assuming only the prismatic, extension twinning and $\langle c + a \rangle$ pyramidal slip modes are shown in Figs. 15 (a2), (b2), and (c2), respectively. Near grain boundary shears are allowed by setting $H = 2$. Only the diagonal effective strain components are imposed in these simulations; all redundant shears are taken to be zero. The asymmetry parameter A is calculated following Eq. (23), and shown against each ODF section. While the experimentally observed fibers shown in Figs. 15 (a1), (b1), and (c1) are predicted at all the three sections shown in Figs. 15 (a2), (b2), and 15 (c2), the predicted

asymmetry parameter A does not agree even in sign with the experimental value at the near rolls and center sections. Negligible asymmetry in the final texture is predicted at all three sections, with the least at the near mandrel section, whereas considerable asymmetry is measured therein (Figs. 15 (a1), (b1), and (c1)).

The role of imposed non-diagonal redundant shears (Eq. (19)) is considered next. In the present work, each allowable redundant shear is separately imposed. Imposition of components $L_{PD,ND} = \pm Q$, or $L_{PD,TD} = \pm Q$, or $L_{TD,PD} = \pm Q$ results in texture predictions (not shown) that are qualitatively much too different from experimental observations: the predictions do not capture even the experimentally observed texture fibers. This suggests that these redundant shear components are physically unrealistic. However, when $L_{TD,ND} = \pm Q$ is imposed, the three fibers in the final texture are retained and a non-zero asymmetry develops.

Figs. 15 (a3), (b3), and (c3) are the final ODF sections predicted by imposing $L_{TD,ND} = -Q$ at the near rolls and center sections and $L_{TD,ND} = Q$ at the near mandrel section. The asymmetry parameters A of the predicted textures are also indicated in the figure. It is not attempted to quantitatively match the predicted A with the experimental one. Nevertheless, it is clear that the asymmetry parameters in Figs. 15 (a3), (b3), and (c3) obtained by imposing a redundant shear agree better (at least in sign) with the experimental observation than those obtained in Figs. 15 (a2), (b2), and (c2), without redundant shears. It is also clear that imposing a negative redundant shear $L_{TD,ND} \leq 0$ increases A , and conversely, imposing a positive $L_{TD,ND} \geq 0$ redundant shear decreases A .

The sign change in $L_{TD,ND}$ between the near rolls and near mandrel sections suggests that frictional shear forces predominantly directed toward $\pm TD$ are exerted by the pilger mill tooling (rolls and mandrel) on the tube. The opposite sign of A at the near rolls and mandrel sections suggests that the TD frictional force between the rolls and tube is directed opposite to that between the mandrel and the tube.

The larger absolute asymmetry parameters at the near roll and near mandrel sections than at the center indicate that the total redundant shear, and hence, total deformation experienced by material points at the tube surfaces is larger than that in the bulk. This conclusion is also consistent with the larger GAM values observed at the tube surfaces reported in Sec. V A 1.

In their studies on redundant shears in pilgering using inserts, Girard et al. [21] found that the most significant redundant shear components were $L_{PD,ND}$ and $L_{ND,PD}$. The important redundant shear in the present work, $L_{TD,ND}$, differs from those found by Girard et al. [21]. This shows that the important redundant shear component in pilgering is not universal. Instead, the important redundant shear components appear to be specific to the pilgering die and tube pair.

3. Q Variation

A difference between the present modeling work and foregoing ones [21,36] is that whereas the present simulations impose a close approximation of the actual deformation with axial position (Fig. 5 (c)), foregoing works imposed a uniform \bar{Q} for each pilgering pass determined from the initial and final dimensions of the tube. For the present tube, imposed pilgering strains reduce the outer radius of the tube from $R_0 = 25$ mm to $R = 14$ mm, while the change in the inner radius is from $r_0 = 17$ mm to $r = 11$ mm. Tube thickness thus reduces from 8 mm to 3 mm. Substituting $\rho_0 = R_0$ and $\rho = R$ in Eq. (14) yields $\bar{Q} = 1.59$ at the near roll mesoscale material point. Similarly, $\bar{Q} = 1.89$ and $\bar{Q} = 2.44$ are obtained at the center and at the near mandrel material points, respectively.

Fig. 16 compares the final textures predicted by imposing the actual axial position dependent Q with that obtained by imposing a uniform \bar{Q} at the center section. Final textures, slip activities and deformation distribution in the grains are found to be largely similar in the two cases. This leads us to conclude that the texture predictions are fairly insensitive to the details of the strain-path experienced by the tube.

VI. DISCUSSION

A systematic study of microstructure and texture evolution in a partly pilgered tube has been performed. Pilgering is observed to homogenize the microstructure by making the grain sizes and aspect ratios comparable through the thickness. In accord with experimental observations reported in the literature, pilgering is also found to intensify the (0002), $\langle 1\bar{1}00 \rangle$ and $\langle \bar{1}100 \rangle$ fibers. The asymmetry in the relative intensities of the $\langle 1\bar{1}00 \rangle$ and $\langle \bar{1}100 \rangle$

fibers has been emphasized and quantified by the parameter A in this work. This asymmetry is linked to $\pm ND$ asymmetries in experimental X-ray pole figures.

Texture comparisons between the experimental observations and those obtained from simulations using the binary-tree based polycrystal plasticity model have been performed to test several hypotheses about the physical micro-mechanisms activated. The comparisons show that contraction twinning is not significantly activated, and that accommodative near grain boundary shear is very important in the present material. The latter observation is consistent with recent experimental observations [54]. The sign of the experimentally observed asymmetry parameter A is the signature of the direction of frictional shear forces exerted by the rolls and mandrel on the tube. It is found that these forces have opposite senses at the rolls and mandrel sections.

In summary, the following observations can be made about the flow field. First, qualitative agreement between the experimental and predicted final texture suggests that the metal flow pattern in pilgering is well approximated as $L_{TD,ND}$, simple shear superposed on steady gross axisymmetric flow through a convergent channel. Second, both magnitude and sign of the shear component vary with through thickness location. This is corroborated by the observation that closest agreement of the predicted and experimental post-pilgering texture at the near roll, center and near mandrel sections is obtained by superposing positive, positive and negative imposed redundant shear $L_{TD,ND}$, respectively, over the gross flow. Finally, the amplitude of the varying $L_{TD,ND}$ simple shear is comparable to the normal/effective strains. This follows from the observation that prediction of the textural asymmetries observed experimentally requires the imposition of $L_{TD,ND}$, of the order of Q .

Predictions of the post-pilgering texture using the VPSC [47] model in the literature [21,36] have succeeded in capturing the peak intensity of either the $\{0002\}$ or the $\{1\bar{1}00\}$ pole figures. Lebensohn et al. [36] capture the peak intensity of the $\{1\bar{1}00\}$ pole figure, while overestimating the peak $\{0002\}$ pole intensity after one pass. Girard et al. [21] on the other hand, overestimate the peak intensity of the $\{1\bar{1}00\}$ pole figures, while capturing the peak $\{0002\}$ pole intensity.

In contrast to the aforementioned works, the present predictions uniformly underestimate the experimentally observed peak pole or ODF intensities. This may be attributed to both physical and modeling reasons. First, the strain-path that the physical material point experiences

is highly non-monotonic and will involve several partial reversals in the direction of the redundant strain-rates. This implies that the physical material point during non-monotonic pilgering experiences much larger total strain than the simulated material point that undergoes only monotonic deformation. Accounting for the larger strain along a non-monotonic path will lead to texture intensification in the simulations and produce better agreement with experiments. Second, a microscopic mechanism that is likely to be highly important in the present material is grain fragmentation, as suggested by the observations of Sahoo et al. [77,78,80] in Zircaloy-2. Grain fragmentation initiates with banding. Subsequent divergence of lattice orientations in neighboring bands with deformation results in large misorientation development and grain refinement [59]. Banding is known to modify the texture qualitatively, and to enhance the texturing rate of certain texture components [81]. More significantly, when grain refinement occurs during processes wherein the strain-path is not monotonic, texture developed during the forward pass is substantially retained even after reversal [82,83]. Finally, lattice rotations in the binary-tree based model occur about rotation axes that are more dispersed [38,84] on the surface of the unit sphere than in mean-field models such as VPSC. This is because, whereas in the binary tree based model immediate neighbors of grains significantly influence their lattice rotations, in VPSC, the rotations of all grains are determined by compatibility with a common homogeneous effective medium.

VII. CONCLUSIONS

The production of zirconium alloy tubes used in the nuclear industry often involves a series of cold pilgering and annealing steps [40]. Pilgering, a relatively complex forming technique [3], leads to developments in deformed microstructure and crystallographic texture. The present partly pilgered specimen allows experimental study of these developments at different through-thickness and axial positions during a single pilgering step. Pilgering is found to homogenize the microstructure, and to produce texture intensification of the (0001), $\langle \bar{1}100 \rangle$, and $\langle 1\bar{1}00 \rangle$ fibers. The unequal intensification of the latter two fibers is quantified using a scalar asymmetry parameter, A . This asymmetry is not reflected in the evolution of the Kearns factors.

Polycrystal plasticity simulations based on the binary-tree based model are used to understand texture development and the pattern of metal flow during pilgering. It is found that despite pilgering being a complex unsteady incremental deformation process, a qualitatively acceptable prediction of the pilgering texture is obtained using a simple metal flow pattern, which is a superposition of steady axisymmetric extrusion and location-dependent lateral frictional transverse shear, provided the appropriate grain-level slip and twinning modes, near grain boundary deformation, and location-dependent frictional shear, are duly accounted for. The predicted texture intensities are, however, smaller than those experimentally measured. This is ascribed to non-accounting for the extensive grain fragmentation and for the non-monotonic deformation path, in the physical tube. The sign of the measured asymmetry parameter informs the direction of the transverse frictional force. Frictional forces acting on the outer and inner o tube surfaces are oppositely directed.

ACKNOWLEDGMENTS

This research is supported by the Board of Research in Nuclear Science (BRNS) and by the National Facility of Texture and OIM, a DST-IRPHA facility at IIT Bombay.

REFERENCES

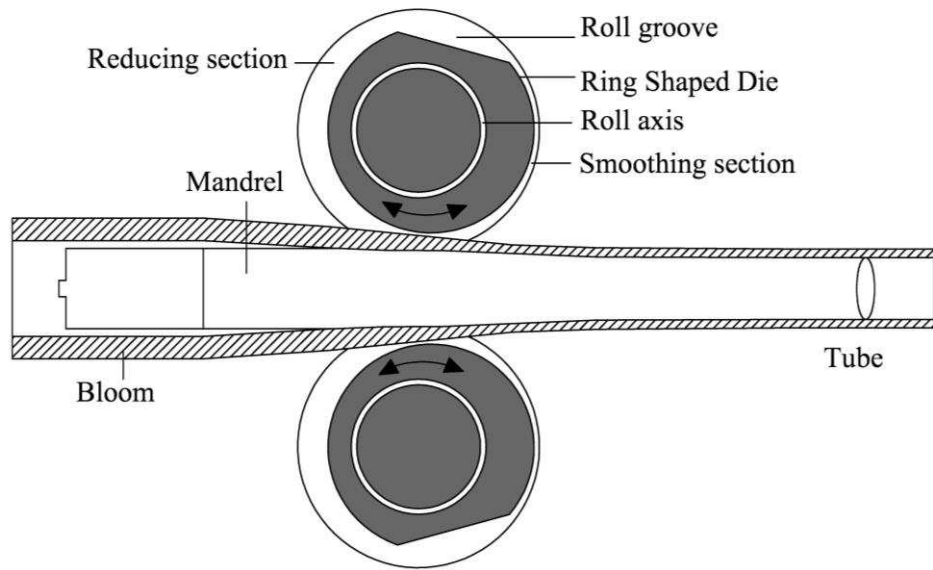
- [1] O. Strehlau: *Tube Pipe J.*, 2006, pp. 1–4.
- [2] J. Osika, H. Palkowski, K. Swiatkowski, D. Pociecha, and A. Kula: *Arch. Metall. Mater.*, 2009, vol. 54, pp. 1239–51.
- [3] B. Verlinden, J. Driver, I. Samajdar, and R.D. Doherty: *Thermo-Mechanical Processing of Metallic Materials*, 2007, pp. 289–97.
- [4] B.A. Cheadle, C.E. Ells, and W. Evans: *J. Nucl. Mater.*, 1967, vol. 23, pp. 199–208.
- [5] E. Tenckhoff: *ASTM Spec. Tech. Publ. 966*, 1988, pp. 1–77.
- [6] N. Saibaba: *J. Nucl. Mater.*, 2008, vol. 383, pp. 63–70.
- [7] H. Abe, L.K. Takeda, A. Uehira, H. Anada, and M. Furugen: *ASTM Spec. Tech. Publ. 1354*, 2000, pp. 425–59.
- [8] H. Abe and M. Furugen: *J. Mater. Process. Technol.*, 2012, vol. 212, pp. 1687–93.

- [9] A. Gaillac, C. Lemaignan, and P. Barberis: *J. ASTM Int.*, 2011, vol. 8, pp. 1–16.
- [10] C.S. Cook, G.P. Sabol, K.R. Sekera, and S.N. Randall: *ASTM Spec. Tech. Publ. 1132*, 1991, pp. 80–95.
- [11] E. Tenckhoff: *J. ASTM Int.*, 2005, vol. 2, pp. 1–26.
- [12] S.S. Bhadauria, M.S. Hora, and K.K. Pathak: *J. Solid Mech.*, 2009, vol. 1, pp. 226–32.
- [13] R.W. Davies, M.A. Khaleel, W.C. Kinsel, and H.M. Zbib: *J. Eng. Mater. Technol.*, 2002, vol. 124, pp. 125–34.
- [14] Y. Choi, E.J. Shin, and H. Inoue: *Phys. B*, 2006, vol. 385-386, pp. 529–31.
- [15] V.M. Allen, M. Preuss, J.D. Robson, and R.J. Comstock: *Mater. Sci. Forum*, 2005, vol. 495-497, pp. 675–80.
- [16] R. Krishnan and M.K. Asundi: in *Proc. Indian Acad. Sci. (Engg. Sci.) Vol. 4, Pt. 1*, 1981, pp. 41–56.
- [17] E. Tenckhoff and P.L. Rittenhouse: *ASTM Spec. Tech. Publ. 458*, 1969, pp. 50–67.
- [18] G. Dressler, K.H. Matucha, and P. Wincierz: *Can. Metall. Q.*, 1972, vol. 11, pp. 177–84.
- [19] K. Kallstrom: *Can. Metall. Q.*, 1972, vol. 11, pp. 185–98.
- [20] Y. Choi and H. Inoue: *Mater. Trans.*, 2010, vol. 51, pp. 652–58.
- [21] E. Girard, R. Guillen, P. Weisbecker, and M. Francois: *J. Nucl. Mater.*, 2001, vol. 294, pp. 330–38.
- [22] R. Guillen, C. Cossu, M. Franc, and E. Girard: *J. Nucl. Mater.*, 1998, vol. 255, pp. 174–79.
- [23] R. Guillen, J.L. Feron, J.L. Glimois, F. Hunt, J. Le Pape, and J. Senevat: *Textures Microstruct.*, 1991, vol. 14-18, pp. 519–24.
- [24] N.P. Gurao, H. Akhiani, and J.A. Szpunar: *J. Nucl. Mater.*, 2014, vol. 453, pp. 158–68.
- [25] P.S. Godavarti, S. Hussien, and K. Linga Murty: *Metall. Trans. A*, 1988, vol. 19A, pp. 1243–55.
- [26] K.V. Mani Krishna, A. Sain, I. Samajdar, G. Dey, D. Srivastava, S. Neogy, R. Tewari, and S. Banerjee: *Acta Mater.*, 2006, vol. 54, pp. 4665–75.
- [27] R.P. Marshall: *J. Nucl. Mater.*, 1967, vol. 24, pp. 49–59.

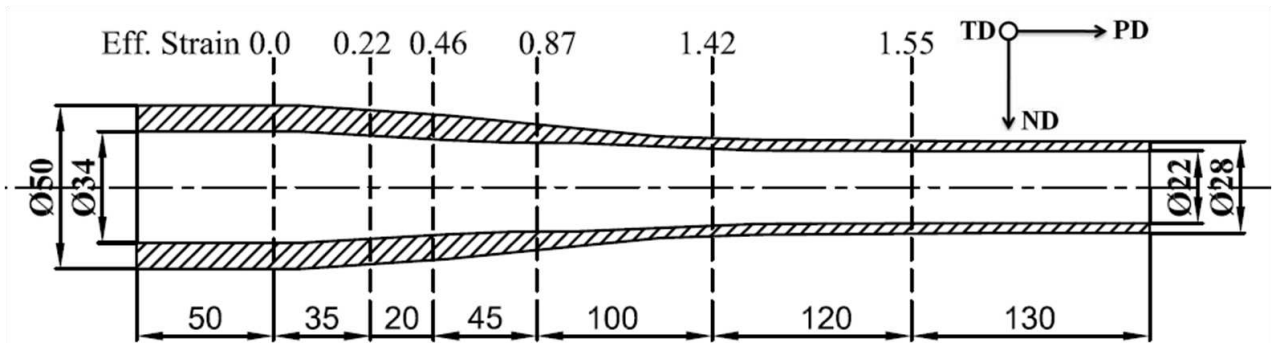
- [28] K. Vaibhaw, S.V.R. Rao, S.K. Jha, N. Saibaba, and R.N. Jayaraj: *J. Nucl. Mater.*, 2008, vol. 383, pp. 71–77.
- [29] S. R. MacEwen and C. Tome: *ASTM Spec. Tech. Publ. 939*, 1987, pp. 631–50.
- [30] M. Furugen and C. Hayashi: *J. Mech. Work. Technol.*, 1984, vol. 10, pp. 273–86.
- [31] J.L. Aubin, E. Girard, and P. Montmitonnet: *ASTM Spec. Tech. Publ. 1245*, 1994, pp. 245–63.
- [32] S. Mulot, A. Hacquin, P. Montmitonnet, and J.-L. Aubin: *J. Mater. Process. Technol.*, 1996, vol. 60, pp. 505–12.
- [33] P. Montmitonnet, R. Loge', M. Hamery, Y. Chastel, J.-L. Doudoux, and J.-L. Aubin: *J. Mater. Process. Technol.*, 2002, vol. 125-126, pp. 814–20.
- [34] B. Lodej, K. Niang, P. Montmitonnet, and J.-L. Aubin: *J. Mater. Process. Technol.*, 2006, vol. 177, pp. 188–91.
- [35] M. Harada, A. Honda, and S. Toyoshima: *J. ASTM Int.*, 2005, vol. 2, pp. 1–14.
- [36] R.A. Lebensohn, M.I. Gonzalez, C.N. Tome, and A.A. Pochettino: *J. Nucl. Mater.*, 1996, vol. 229, pp. 57–64.
- [37] U.F. Kocks, C.N. Tomé, and H.-R. Wenk: *Texture and Anisotropy*, Cambridge University Press, Cambridge, U.K., 1998.
- [38] S. Mahesh: *Int. J. Plast.*, 2009, vol. 25, pp. 752–67.
- [39] Y. Choi and H. Inoue: *Mater. Sci. Forum*, 2007, vol. 558-559, pp. 1379–82.
- [40] K.V. Mani Krishna, S.K. Sahoo, I. Samajdar, S. Neogy, R. Tewari, D. Srivastava, G.K. Dey, G. H. Das, N. Saibaba, and S. Banarjee: *J. Nucl. Mater.*, 2008, vol. 383, pp. 78–85.
- [41] F. E. Hauser, P. R. Landon, and J. E. Dorn: *Trans. ASM*, 1956, vol. 48, pp. 986–1002.
- [42] B.D. Cullity and S.R. Stock: *Elements of X-Ray Diffraction, 3rd Edition*, Prentice Hall, New Jersey, 2001, pp. 416–21.
- [43] D. Raabe and K. Lücke: *Phys. Status Solidi*, 1993, vol. 180, pp. 59–65.
- [44] M.M. Nowell and S.I. Wright: *Ultramicroscopy*, 2005, vol. 103, pp. 41–58.
- [45] T.H. Cormen, C.E. Leiserson, R.L. Rivest, and C. Stein: *Introduction to Algorithms*, Third Edit, MIT press, Cambridge, 2009.

- [46] G.I. Taylor: *J. Inst. Met.*, 1938, vol. 62, pp. 307–24.
- [47] R.A. Lebensohn and C.N. Tomé: *Acta Met. Mater.*, 1993, vol. 41, pp. 2611–24.
- [48] C.N. Tome, P.J. Maudlin, R.A. Lebensohn, and G.C. Kaschner: *Acta Mater.*, 2001, vol. 49, pp. 3085–96.
- [49] J.W. Christian and S. Mahajan: *Prog. Mater. Sci.*, 1995, vol. 39, pp. 1–157.
- [50] G.Y. Chin, W.F. Hosford, and D.R. Mendorf: *Proc. of R. Soc. London*, 1969, vol. 309, pp. 433–56.
- [51] L. Wang, Y. Yang, P. Eisenlohr, T.R. Bieler, M.A. Crimp, and D.E. Mason: *Metall. Mater. Trans. A*, 2010, vol. 41, pp. 421–30.
- [52] L. Capolungo, P.E. Marshall, R.J. McCabe, I.J. Beyerlein, and C.N. Tomé: *Acta Mater.*, 2009, vol. 57, pp. 6047–56.
- [53] M. A. Meyers and E. Ashworth: *Phil. Mag. A*, 1982, vol. 46, pp. 737–59.
- [54] N. Keskar, S. Mukherjee, K.V. Mani Krishna, D. Srivastava, G.K. Dey, P. Pant, R.D. Doherty, and I. Samajdar: *Acta Mater.*, 2014, vol. 69, pp. 265–74.
- [55] P.G. Partridge: *Philos. Mag.*, 1965, vol. 12, pp. 1043–54.
- [56] P.G. Partridge: *Met. Rev.*, 1967, vol. 12, pp. 169–94.
- [57] W.J. McG. Tegart: *Philos. Mag.*, 1964, vol. 9, pp. 339–41.
- [58] M.L. Picklesimer: *J. Electrochem. Soc.*, 1966, vol. 4, pp. 289–300.
- [59] J.L. Martin and R.E. Reed-Hill: *Trans. Met. Soc. AIME*, 1964, vol. 230, pp. 780–85.
- [60] E.J. Rapperport: *Acta Metall.*, 1959, vol. 7, pp. 254–60.
- [61] O. Engler, M. Crumbach, and S. Li: *Acta Mater.*, 2005, vol. 53, pp. 2241–57.
- [62] G. Sachs: *Z. Verein. Deutsch. Ing.*, 1928, vol. 72, pp. 734–47.
- [63] A. Staroselsky and L. Anand: *Int. J. Plast.*, 2003, vol. 19, pp. 1843–64.
- [64] H. Abe, K. Matsuda, T. Hama, T. Konishi, and M. Furugen: *ASTM Spec. Tech. Publ. 1245*, 1994, pp. 285–306.
- [65] J.J. Kearns: *Thermal Expansion and Preferred Orientation in Zircaloy*, Pittsburgh, PA (USA), 1965, p. WAPD – TM – 472.

- [66] K.V. Mani Krishna, D. Srivastava, G.K. Dey, V. Hiwarkar, I. Samajdar, and N. Saibaba: *J. Nucl. Mater.*, 2011, vol. 414, pp. 492–97.
- [67] J.J. Kearns: *J. Nucl. Mater.*, 2001, vol. 299, pp. 171–74.
- [68] R.G. Ballinger and R.M. Pelloux: *J. Nucl. Mater.*, 1981, vol. 97, pp. 231–53.
- [69] J.A. Gruber, S.A. Brown, and G.A. Lucadamo: *J. Nucl. Mater.*, 2011, vol. 408, pp. 176–82.
- [70] K. Linga Murty and I. Charit: *Prog. Nucl. Energy*, 2006, vol. 48, pp. 325–59.
- [71] N. Nagai, T. Kakuma, and K. Fujita: *ASTM Spec. Tech. Publ. 754*, 1982, pp. 26–38.
- [72] T. Konishi, M. Honji, T. Kojima, and H. Abe: *ASTM Spec. Tech. Publ. 939*, 1987, pp. 653–61.
- [73] V. Randle and O. Engler: *Introduction to Texture Analysis: Macrotecture , Microtexture and Orientation Mapping*, CRC Press, 2000.
- [74] K.-H. Kim and D.N. Lee: *Acta Mater.*, 2001, vol. 49, pp. 2583–95.
- [75] J. Sarkar, S. Cao, and S. Saimoto: *Mater. Sci. Forum*, 2005, vol. 495-497, pp. 567–72.
- [76] C.S. Lee, R.E. Smallman, and B.J. Duggan: *Mater. Sci. Technol.*, 1994, vol. 10, pp. 149–54.
- [77] S.K. Sahoo, V.D. Hiwarkar, A. Majumdar, I. Samajdar, P. Pant, G.K. Dey, D. Srivastav, R. Tiwari, and S. Banerjee: *Mater. Sci. Eng. A*, 2009, vol. 518, pp. 47–55.
- [78] S.K. Sahoo, V.D. Hiwarkar, I. Samajdar, P. Pant, G.K. Dey, D. Srivastav, R. Tewari, and S. Banerjee: *Mater. Sci. Technol.*, 2010, vol. 26, pp. 104–14.
- [79] H. Numakura, Y. Minonishi, and M. Koiwa: *Philos. Mag. A*, 1991, vol. 63, pp. 1077–84.
- [80] S. Sahoo, V. Hiwarkar, I. Samajdar, G. Dey, D. Srivastav, R. Tiwari, and S. Banerjee: *Scr. Mater.*, 2007, vol. 56, pp. 963–66.
- [81] C.S. Lee and B.J. Duggan: *Acta Metall. Mater.*, 1993, vol. 41, pp. 2691–99.
- [82] S. Mahesh, I.J. Beyerlein, and C.N. Tomé: *Scr. Mater.*, 2005, vol. 53, pp. 965–69.
- [83] C.F. Gu and L.S. Tóth: *Acta Mater.*, 2011, vol. 59, pp. 5749–57.
- [84] S. Mahesh: *Int. J. Plast.*, 2010, vol. 26, pp. 42–64.

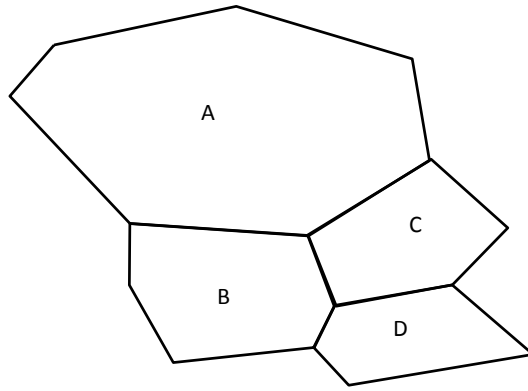


(a)

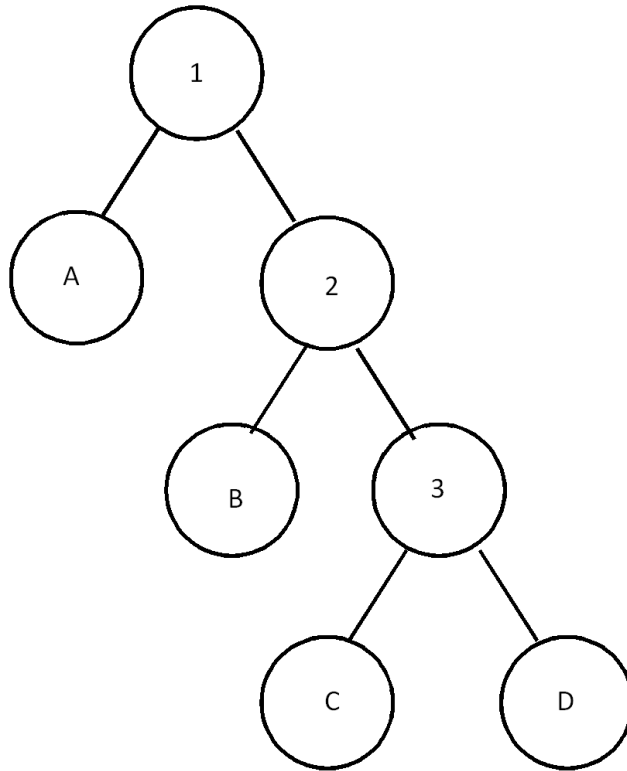


(b)

Figure 1: (a) Schematic drawing of the pilgering process showing the tube (hatched) and the tooling (grooved rolls and mandrel), (b) Photograph and schematic of the present part-pilgered Zircaloy-4 tube showing the sections where microstructure and texture analyses have been performed. All dimensions in mm.



(a)



(b)

Figure 2: Schematic showing (a) a 4-grain microstructure and (b) its representation a binary tree.

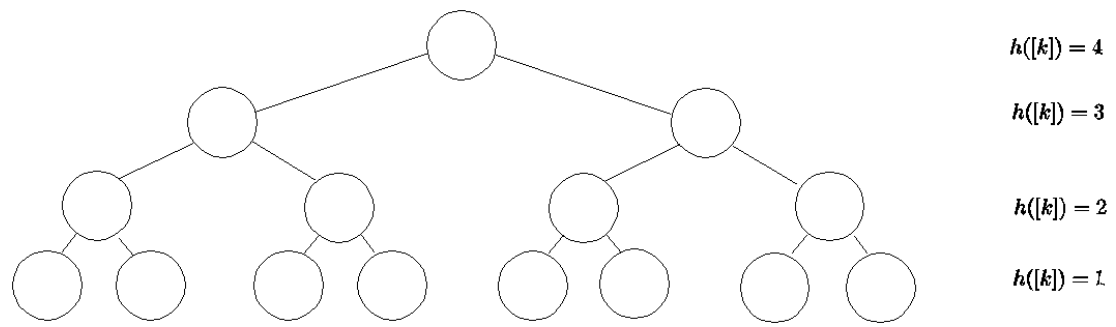


Figure 3: A balanced binary tree representation of an 8-grain polycrystal $h([k])$ is defined in Eq. (6).

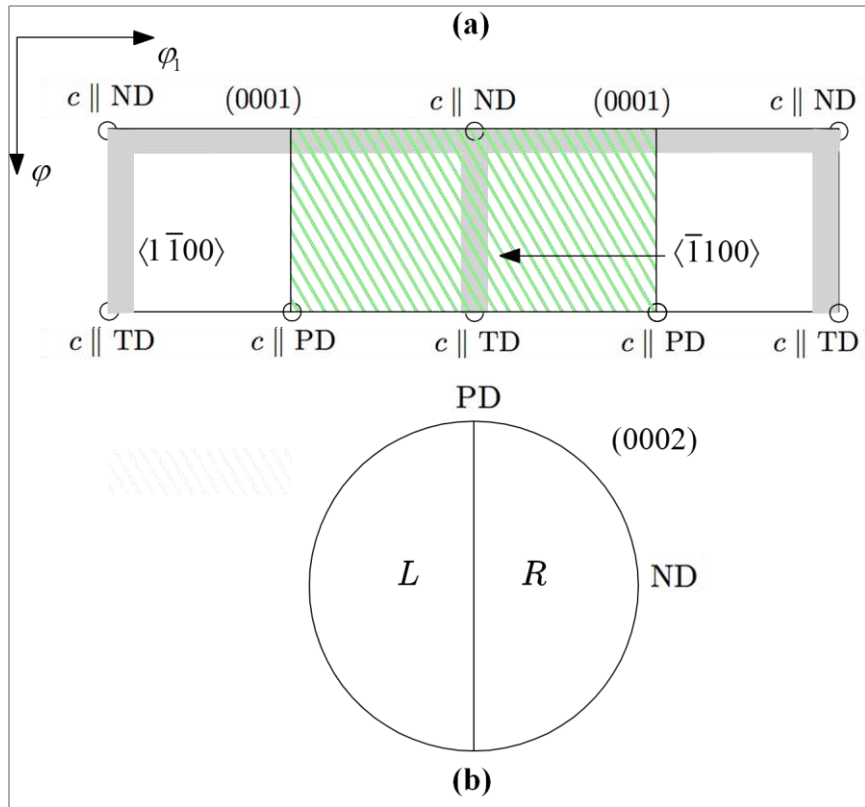
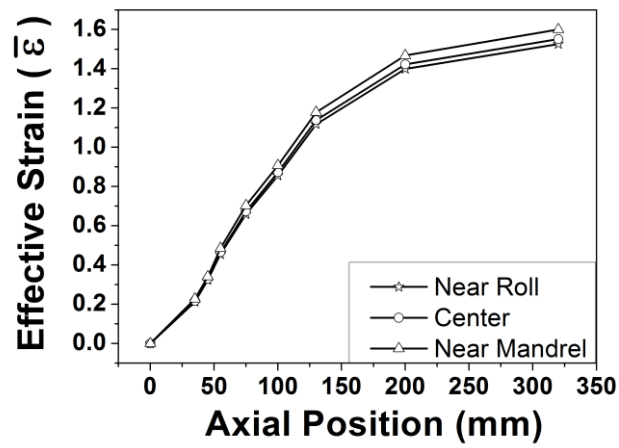
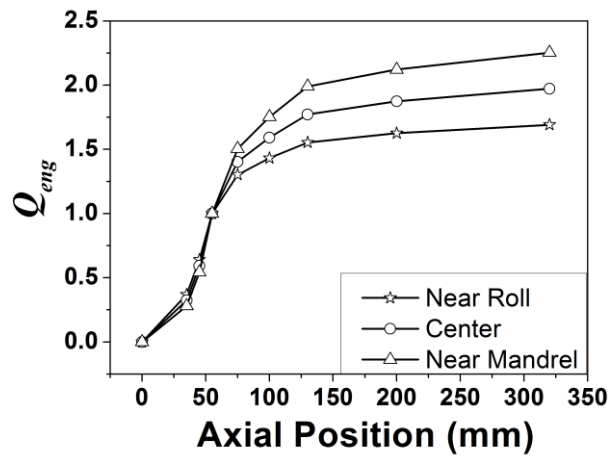


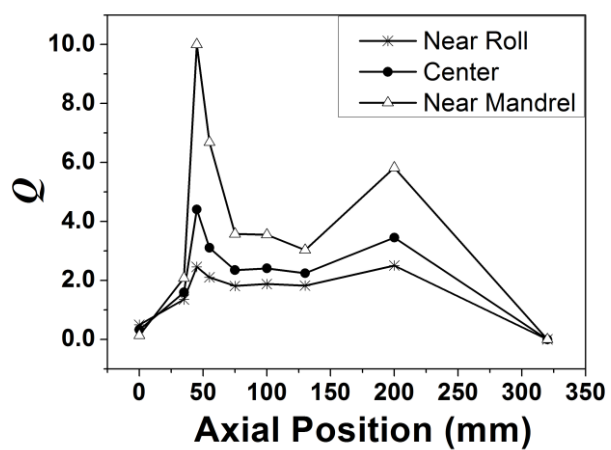
Figure 4: Schematic of a $\varphi_2 = \text{constant}$ ODF section showing the regions corresponding to L (hatched) and R given in Eq. (25).



(a)

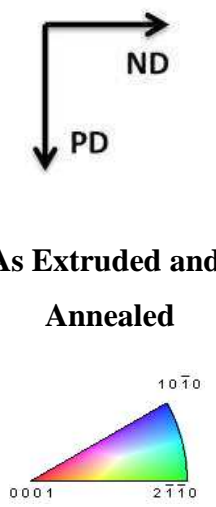
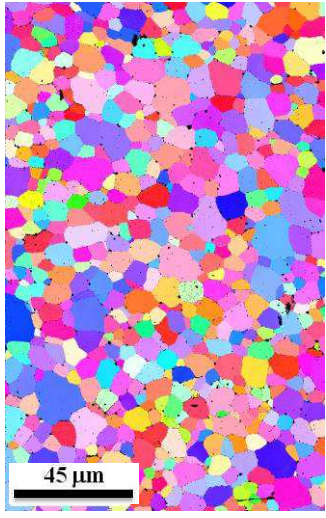
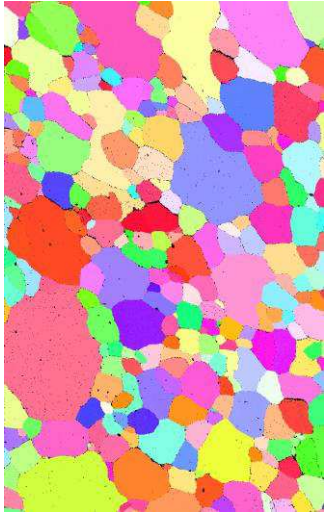
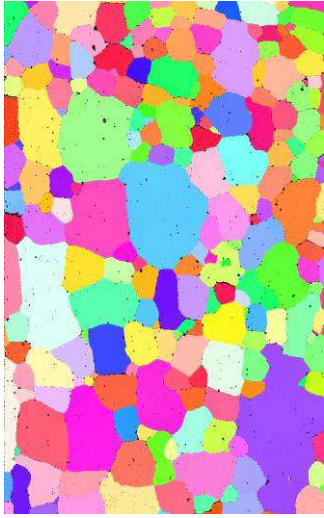
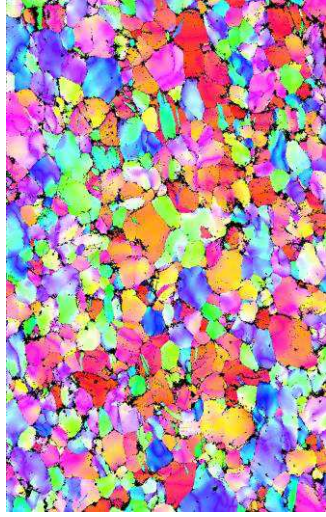
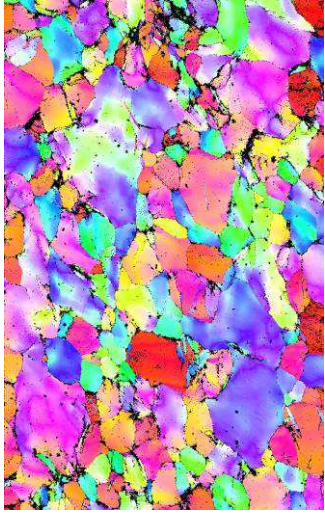
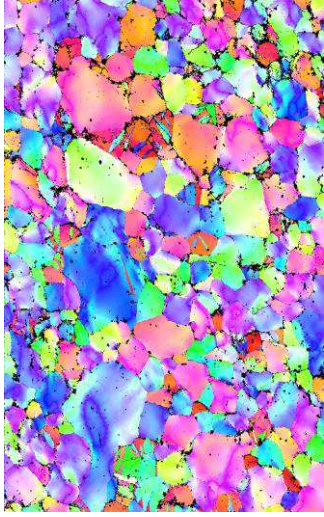
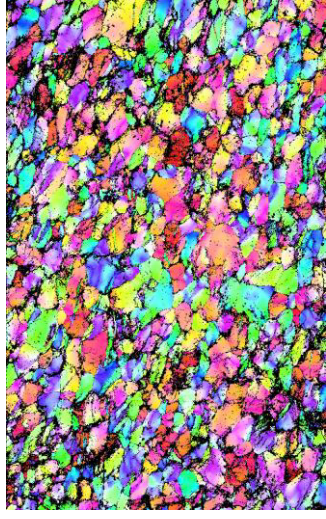
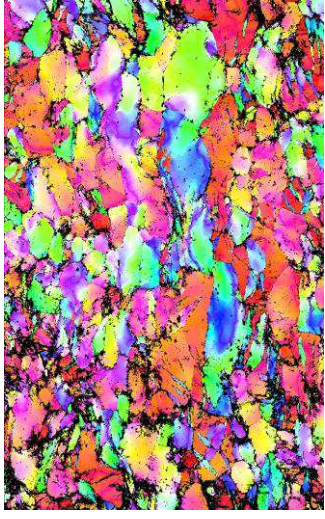
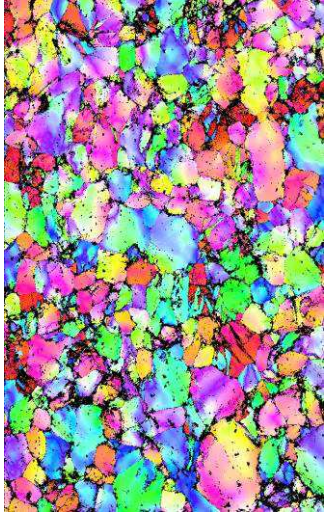


(b)



(c)

Figure 5: (a) Effective strain ($\bar{\epsilon}$) (Eq. (21)), (b) Q_{eng} (Eq. (17)) and (c) Q (Eq. (18)) calculated from specimen dimensions.

Effective Strain ($\bar{\epsilon}$)	Near Roll	Center	Near Mandrel
 <p>As Extruded and Annealed</p>			
0.22			
0.46			

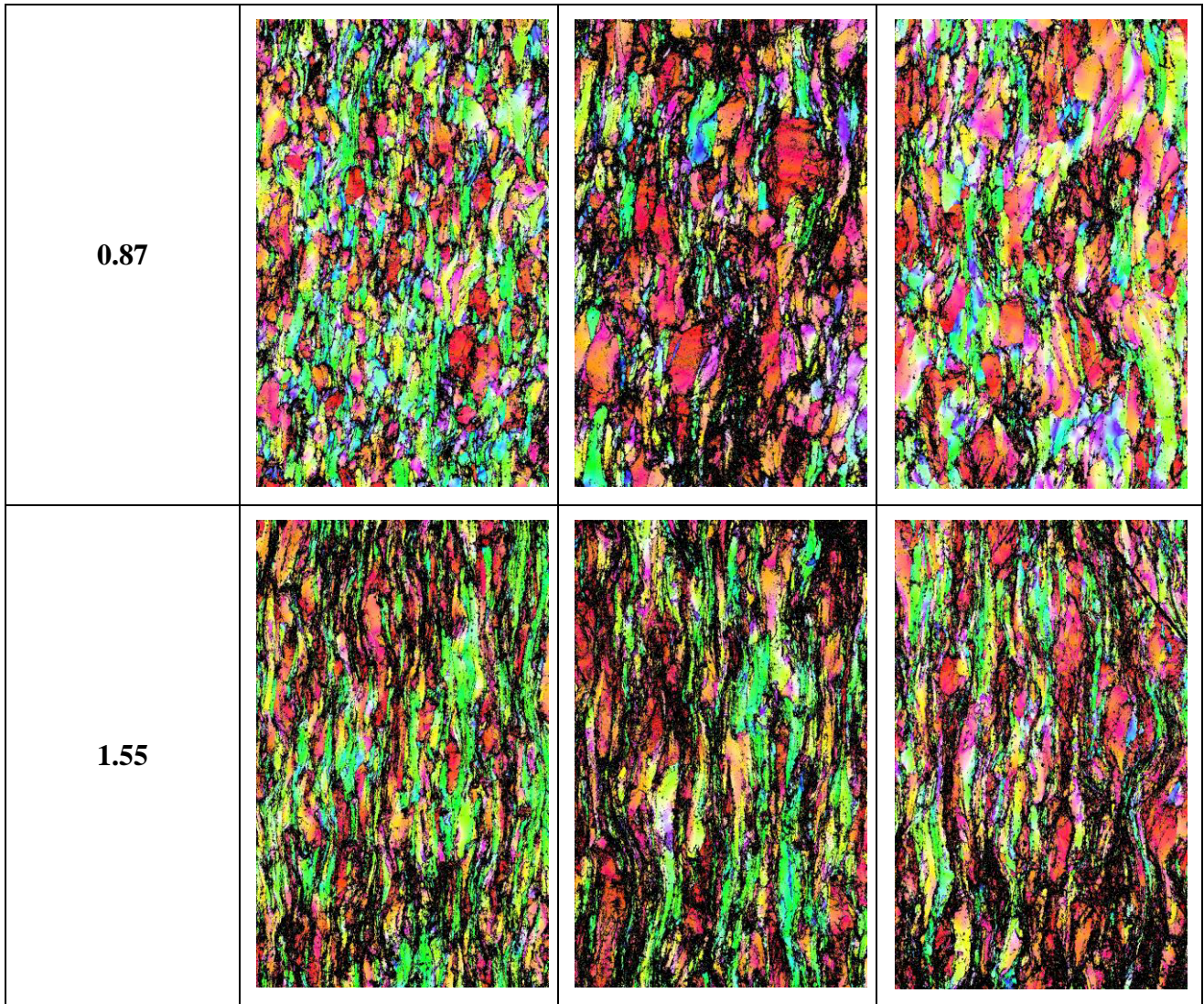
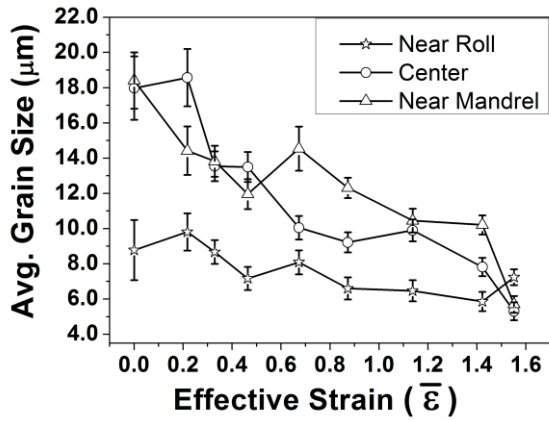
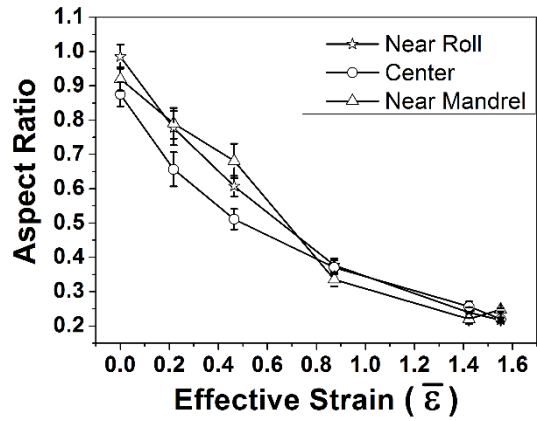


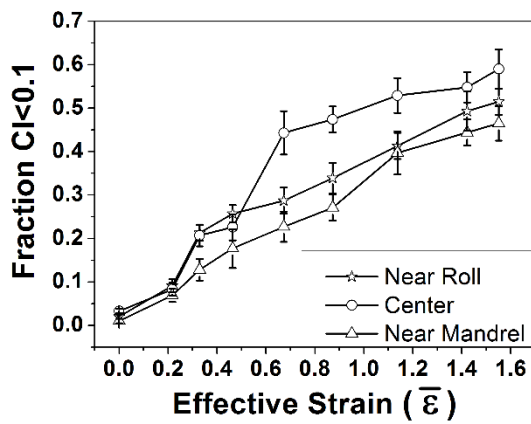
Figure 6: Microstructural developments during pilgering. These are shown as EBSD (electron backscattered diffraction) IPF (inverse pole figure) maps for different effective strains ($\bar{\epsilon}$) and at three through thickness locations: near roll, center and near mandrel. Scans were taken on the long transverse plane (plane containing pilgering (PD) and normal (ND) directions). Black indicates measurement points below 0.1 CI (confidence index). (*Reader may refer the web version for interpretation of color*)



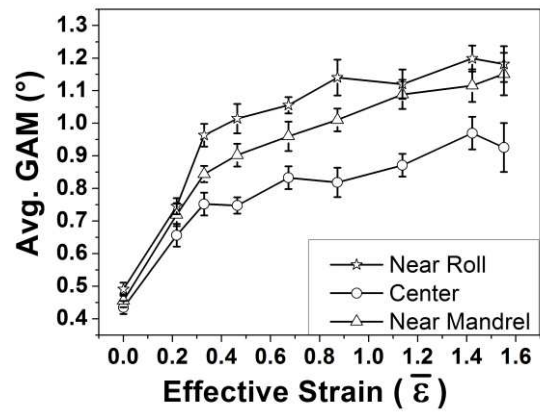
(a)



(b)



(c)



(d)

Figure 7: Variation of the average (a) grain size, (b) grain aspect ratio, (c) CI < 0.1 fraction and (d) GAM (grain average misorientation) with effective strain ($\bar{\epsilon}$). Observations were made at three through thickness locations: near roll, center and near mandrel. Error bars indicating standard deviations derived from multiple EBSD scans are shown.

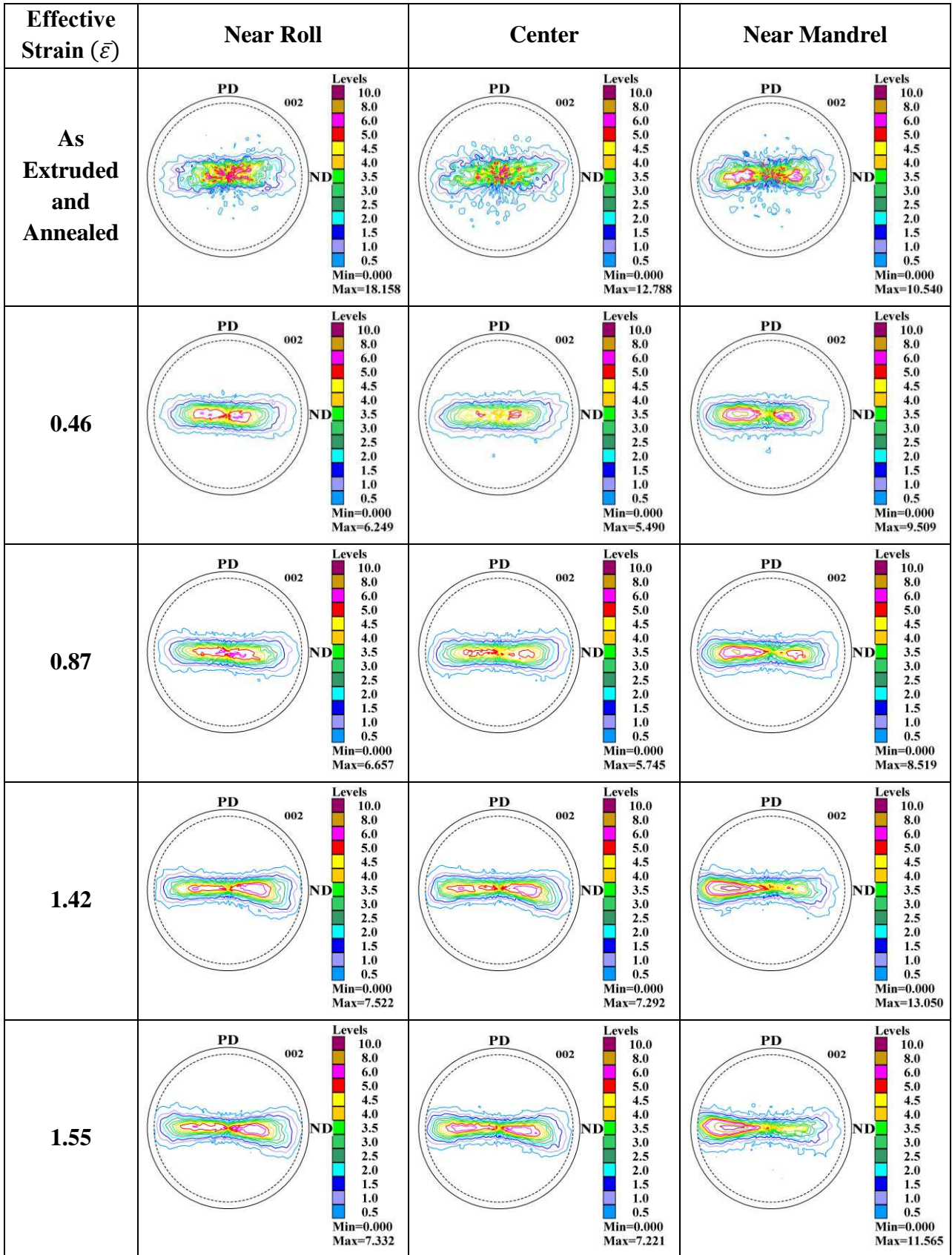


Figure 8: Experimental basal pole figures for different effective strains and different through thickness locations: near roll, center and near mandrel. These were measured by X-ray in the PD-ND long transverse section. (For interpretation/visualization of the color, the reader is referred to the web version of this paper)

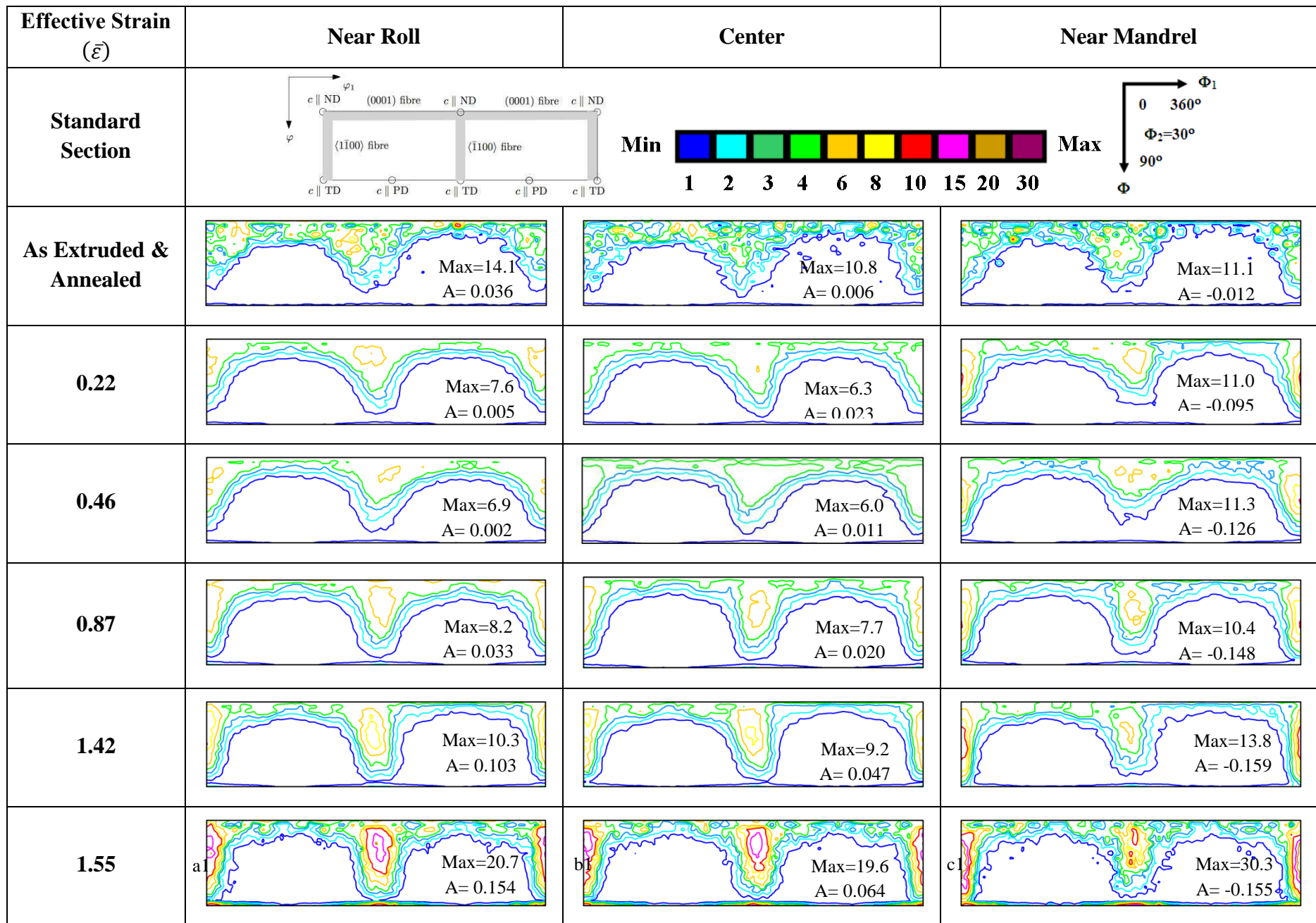
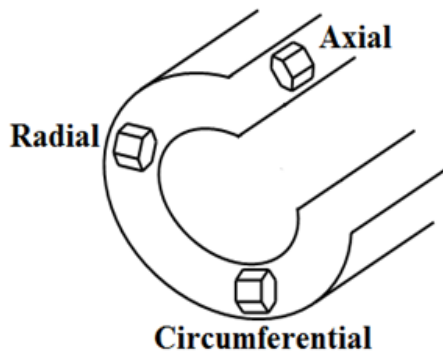
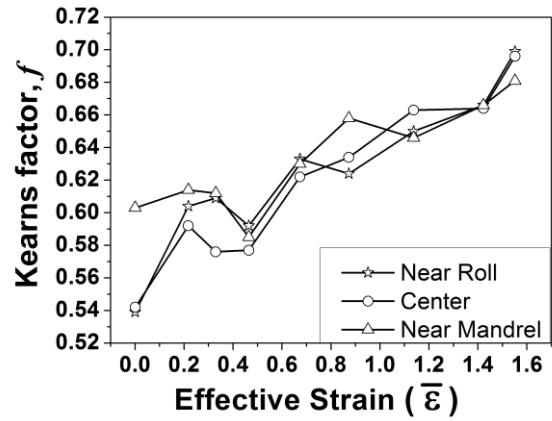


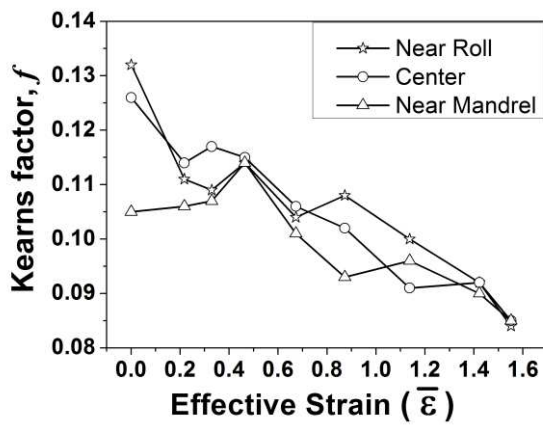
Figure 9: $\varphi_2 = 30^\circ$ ODF sections at different locations and effective strains. These were measured by X-ray bulk texture in the PD-ND long transverse section. Maximum ODF intensity and the asymmetry parameter are marked. Also included is a standard section with the important/idealized crystallographic fibers. (For interpretation/visualization of the color, the reader is referred to the web version of this paper).



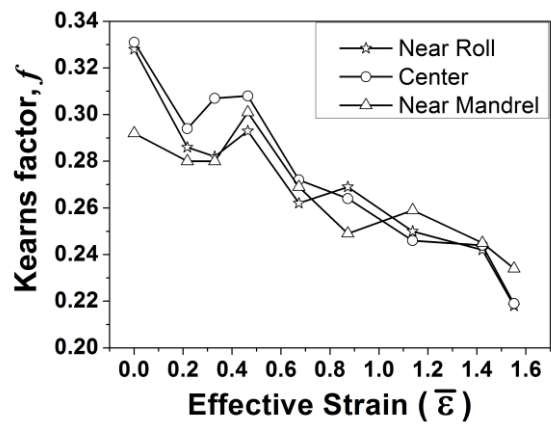
(a)



(b)



(c)



(d)

Figure 10: Evaluation of ODF estimated Kearns factors, f (Eq. (22)) with effective strain ($\bar{\epsilon}$) for (a) Schematic of a tube with unit cells representing basal poles in the three directions (b) Radial, (c) Axial and (d) Circumferential directions.

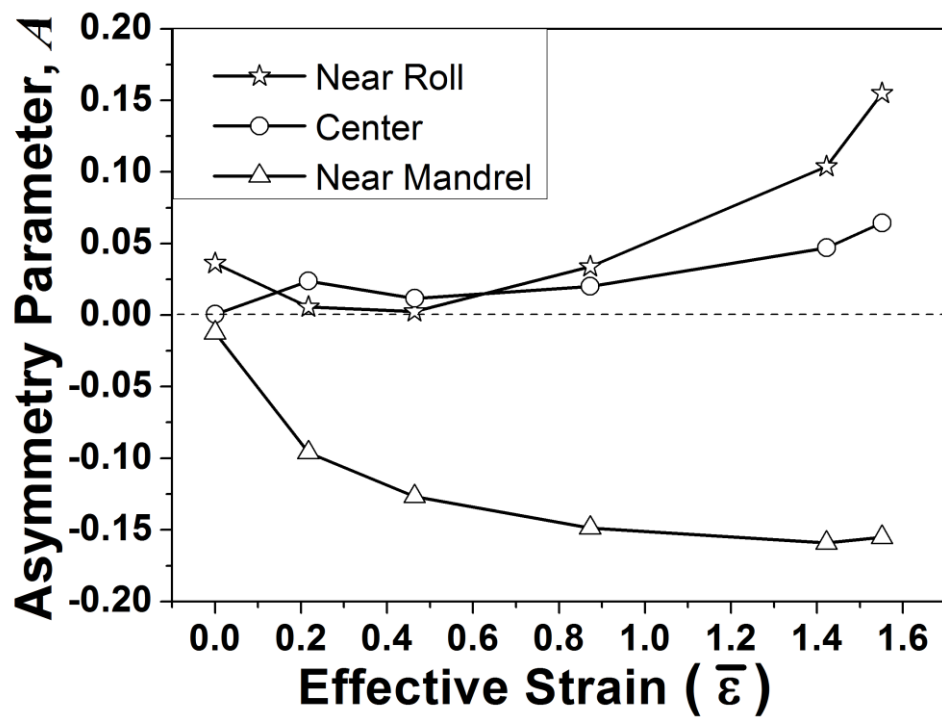


Figure 11: Variation of asymmetry parameter A (Eq. (23)) with effective strain.

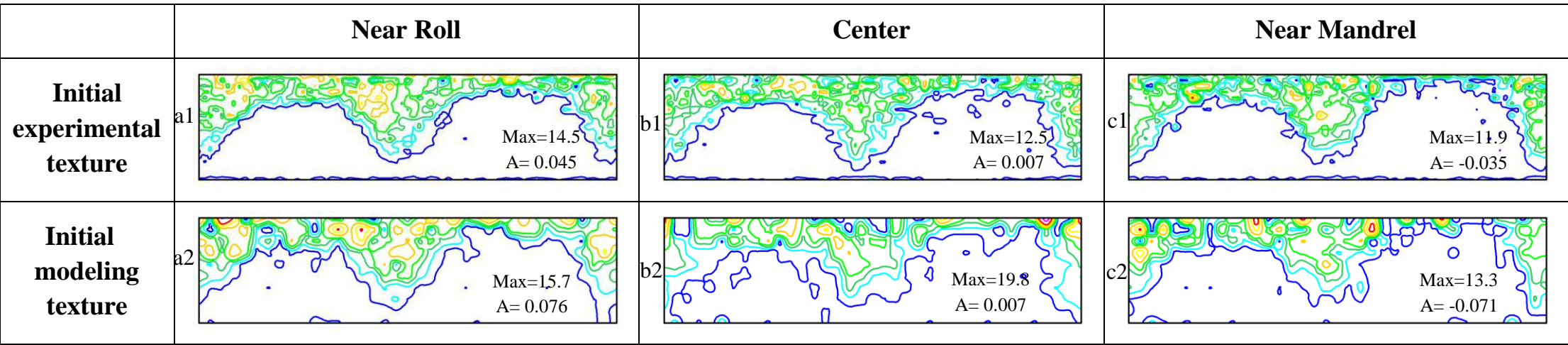


Figure 12: Pre-pilgering $\varphi_2 = 30^\circ$ ODF section. The first row shows the experimental observation at three through thickness locations; the 2nd row is the ODF of the initial discrete texture used in the simulations.

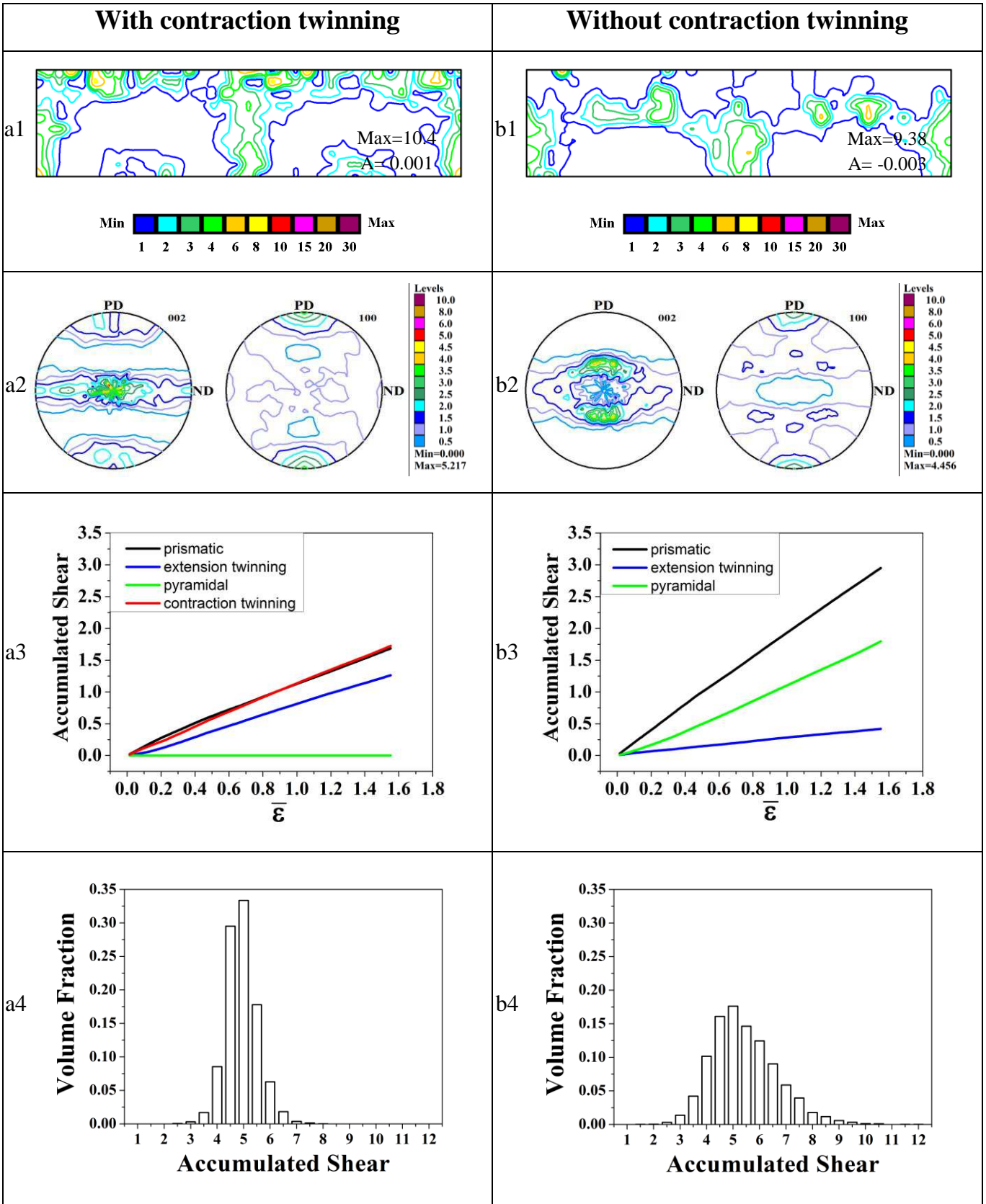


Figure 13: Predicted $\varphi_2 = 30^\circ$ section of the post-pilgering ODF (a1) with (1st column) and (b1) without (2nd column) contraction twinning. The corresponding pole figures are shown in (a2) and (b2), respectively. Average activity of slip and twinning systems per grain are shown in (a3) and (b3). Distribution of the predicted accumulated shear after pilgering is shown in (a4) and (b4).

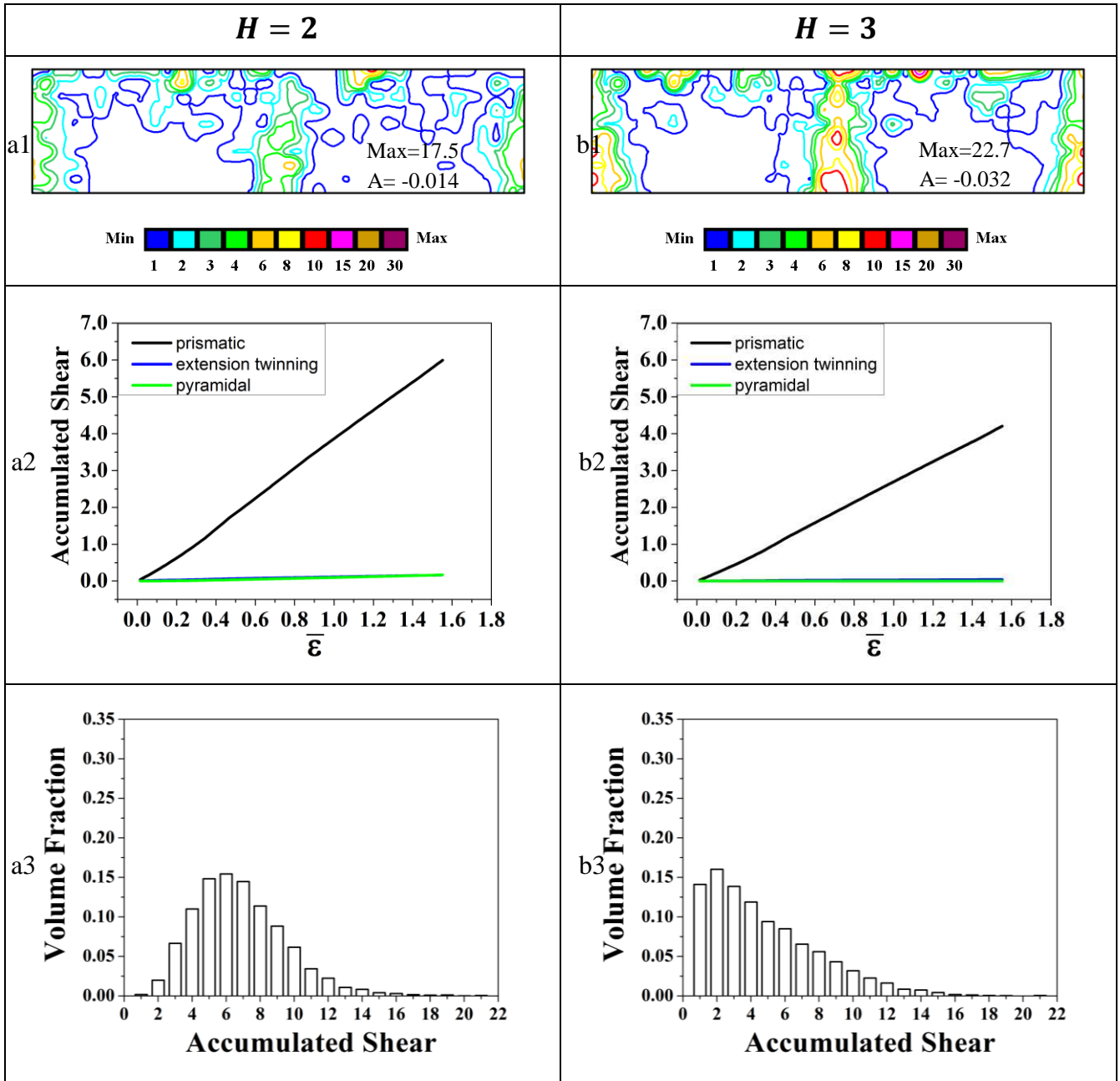


Figure 14: Predicted $\varphi_2 = 30^\circ$ section of the post-pilgering ODF (a1) $H = 2$ (1st column) and (b1) $H = 3$ (2nd column). Average activity of slip and twinning systems per grain are shown in (a2) and (b2). Distribution of the predicted accumulated shear after pilgering is shown in (a3) and (b3).

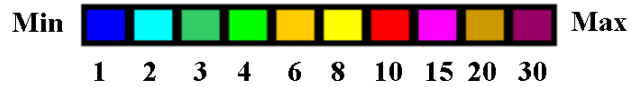
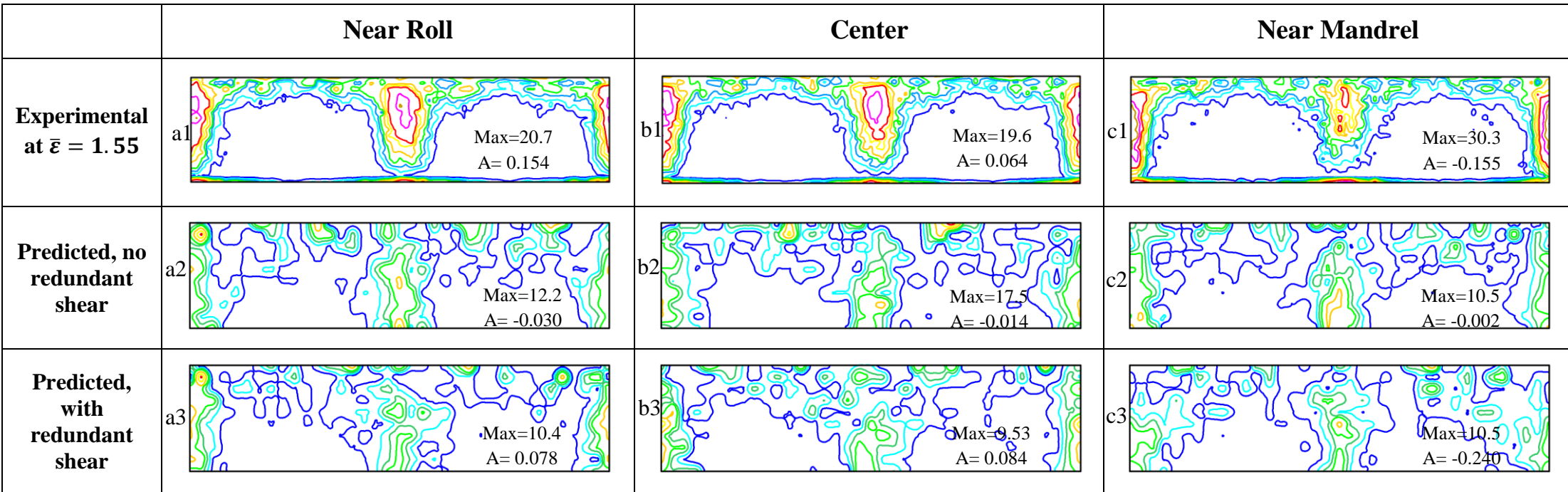


Figure 15: Comparison of the experimental and predicted $\varphi_2 = 30^\circ$ section of the post-pilgering ODF. Experimentally obtained final ODF sections at (a1) near roll, (b1) center and (c1) near mandrel. Predicted final ODF sections at (a2) near roll, (b2) center and (c2) near mandrel, assuming zero redundant shears. Predicted final ODF sections at (a3) near roll assuming $L_{TD,ND} = -Q$, (b3) center, assuming $L_{TD,ND} = -Q$ and (c3) near mandrel, assuming $L_{TD,ND} = +Q$.

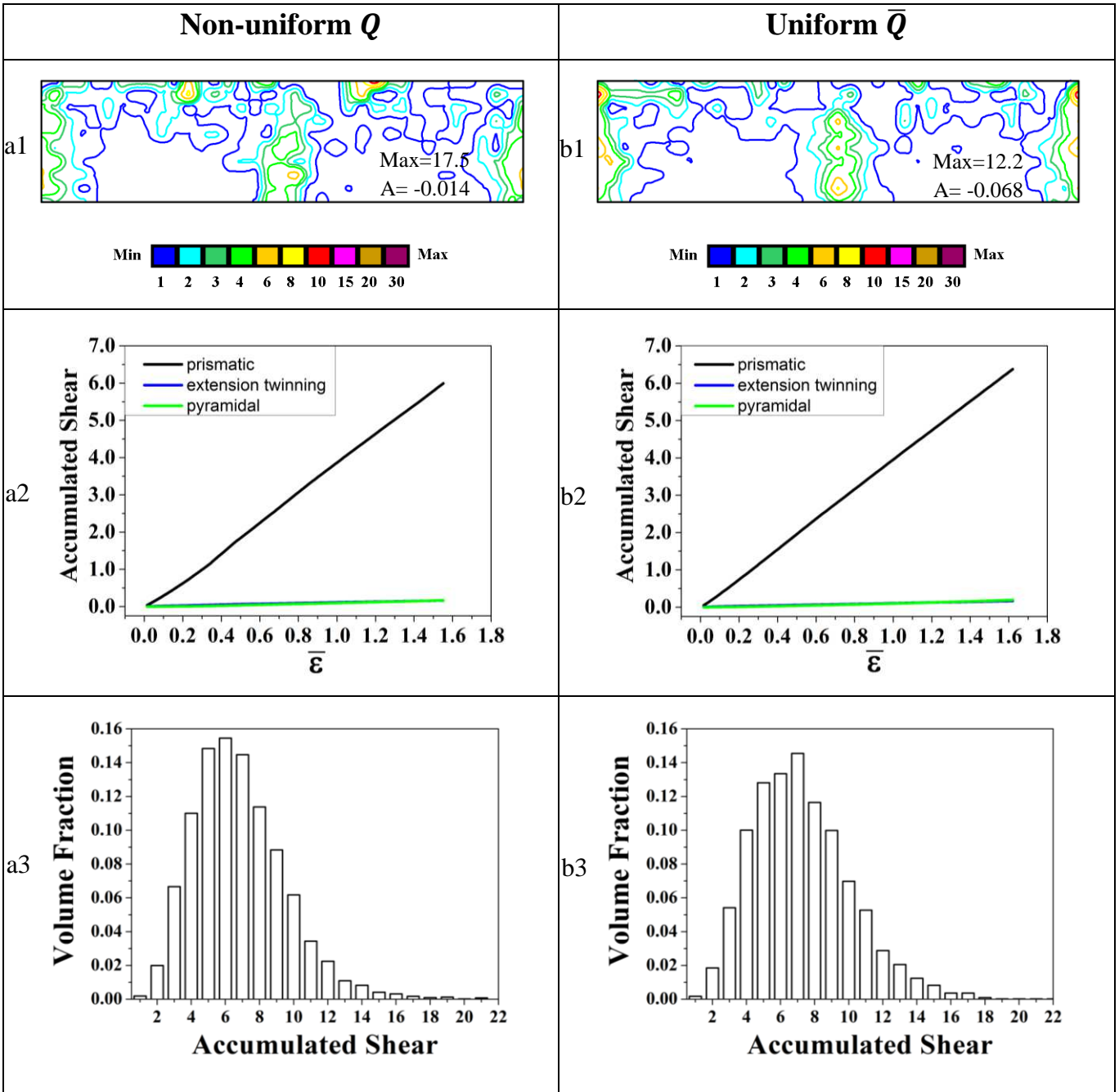


Figure 16: Predicted $\varphi_2 = 30^\circ$ section of the post-pilgering ODF (a1) non-uniform Q (1st column) and (b1) uniform \bar{Q} (2nd column). Average activity of slip and twinning systems per grain are shown in (a2) and (b2). Distribution of the predicted accumulated shear after pilgering is shown in (a3) and (b3).